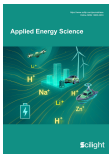
Scilight

Applied Energy Science

https://www.sciltp.com/journals/aes



Article

Optimization of ZnO-AC Nanocomposite Electrodes for Supercapacitor Applications

Prosper Ifeanyichukwu Oghome [1], Innocent Sunday Ike [1,2,*], Eric Egwu Kalu [3], Felicia Lebechukwu Kamen [1], Samson Olufisayo Olubiyi [1], Mesfin Abayneh Kebede [4] and Abdulhakeem Bello [5]

[1] Department of Chemical Engineering, Federal University of Technology, Owerri 460114, Nigeria
[2] African Centre of Excellence in Future Energies and Electrochemical Systems (ACE-FUELS), Federal University of Technology, Owerri 460114, Nigeria
[3] Department of Chemical & Biomedical Engineering, FAMU-FSU College of Engineering, Florida State University, Tallahassee, FL 32310, USA
[4] Institute for Nanotechnology and Water Sustainability (iNanoWS), College of Science, Engineering and Technology (CSET), University of South Africa, Roodepoort 1709, South Africa
[5] Department of Theoretical and Applied Physics, African University of Science and Technology, Abuja 900107, Nigeria
* Correspondence: innocent.ike@futo.edu.ng or innocentsike@gmail.com

How To Cite: Oghome, P.I.; Ike, I.S.; Kalu, E.E.; et al. Optimization of ZnO-AC Nanocomposite Electrodes for Supercapacitor Applications. *Applied Energy Science* **2026**, *1*(1), 9. https://doi.org/10.53941/aes.2026.100009

Received: 11 September 2026
Revised: 14 October 2026
Accepted: 28 October 2026
Published: 12 November 2026

Abstract: The use of rice husk ash, an agricultural-waste-derived feedstock, a potentially greener route to ZnO and activated carbon from unripe plantain peel was considered in the synthesis of ZnO-AC nanocomposite material for electrodes. The ZnO-AC (activated carbon) nanocomposite was prepared in different ratios of as-synthesized ZnO and AC to ascertain the optimum electrode material. The nanocomposites were characterized by scanning electron microscopy (SEM), X-ray diffraction analysis (XRD), and Brunauer-Emmett-Teller analysis (BET) (Micromeritics Instrument Corporation, Norcross, GA, USA). In addition, the electrochemical properties of the prepared nanocomposite electrodes were investigated using cyclic voltammetry (CV), galvanostatic charge-discharge (GCD), and electrochemical impedance spectroscopy (EIS) in 6 M KOH as the electrolyte in a three-electrode setup with nickel foam current collector. The as-prepared ZnO–AC nanocomposite electrodes with ratios of (1:1, 2:1, 3:1, and 4:1) had specific capacitance of 322 F g^{-1}, 113 F g^{-1}, 46.7 F g^{-1}, and 40.7 F g^{-1} at 5 mV s^{-1}, respectively. The electrochemical performance of the ZnO/activated carbon composites is strongly influenced by the ZnO-to-activated carbon ratio. The comparative kinetic investigation proves that electrode performance of the composite material was not governed solely by the quantity of pseudocapacitive zinc oxide added, but rather by the preservation of continuous electronic and ionic percolation pathways. Among the investigated compositions (1:1, 2:1, 3:1 and 4:1), the 1:1 ZnO-AC composite exhibited the optimal structural threshold as it maintains an unblocked porous carbon network for fast ion diffusion (*Rd*2 (finite-length diffusion resistance) = 0.5597 Ω), maximizes pseudocapacitive site utilization without inducing interfacial polarization (*R*2 (charge-transfer resistance) = 4.824 Ω), it synergizes EDLC and pseudocapacitive kinetics (b = 0.58) and delivered the highest specific capacitance from both CV (322 F g^{-1}) at scan rate of 5 mV/s and GCD (227.56 F g^{-1}) at current density of 1 A g^{-1} All the composites maintained good coulombic efficiency around unity and reasonable stability after 3000 cycles.

Copyright: © 2026 by the authors. This is an open access article under the terms and conditions of the Creative Commons Attribution (CC BY) license (https://creativecommons.org/licenses/by/4.0/).
Publisher's Note: Scilight stays neutral with regard to jurisdictional claims in published maps and institutional affiliations.

Keywords: rice husk; zinc oxide; activated carbon; specific capacitance; stability and coulombic efficiency

1. Introduction

Supercapacitors are advanced energy-storage devices that bridge the gap between capacitors and batteries [1]. They are also known as ultracapacitors [2,3] and electrochemical capacitors [4]. Energy storage occurs mainly at the electrode–electrolyte interface, unlike batteries that rely on faradaic reactions [5]. This mechanism enables rapid charge–discharge performance [6] and excellent cycling stability [7]. This process allows supercapacitors to deliver high power densities, rapid charge–discharge rates, and exceptional cycle life, making them attractive for use in hybrid vehicles, renewable energy systems, and portable electronics [4,8]. Supercapacitors are generally classified into three main types: electric double-layer capacitors, pseudo capacitors, and hybrid/asymmetric capacitors [9]. In electric double-layer capacitors, charge storage occurs through ion accumulation on the surface of porous carbon electrodes, forming a Helmholtz double layer without chemical reactions. Pseudo capacitors, in contrast, store energy via fast redox reactions occurring at or near the electrode surface, while hybrid asymmetric capacitors combine both electrostatic and faradaic to achieve improved energy and power balance [8,9].

The performance of the electrode material and the actual device can be analyzed and studied by electrochemical characterization [10]. Cyclic Voltammetry (CV) is usually used to assess capacitive behavior. An ideal electric double-layer capacitor (EDLC) displays a rectangular CV curve, indicating reversible charge storage, while the appearance of small redox peaks suggests pseudo capacitance. Galvanostatic Charge–Discharge (GCD) testing provides information on specific capacitance, energy, and power density, while Electrochemical Impedance Spectroscopy (EIS) evaluates resistance components such as charge transfer resistance and ion diffusion resistance [10,11]. Together, these measurements confirm whether the physical and chemical properties of the material translate effectively into quality electrochemical performance. Generally, materials commonly used as electrodes for the fabrication of supercapacitors include (i) carbon materials that have high surface area, for example, activated carbon, carbon aerogel, carbon nanotubes, graphene, etc (ii) metal oxide/transition metal oxides and hydroxides such as Ru, V, Ni, Mn, Ti, Mo [12], Mg, Fe, Nb, and Co [13]. (iii) conducting polymers like polypyrole (PPy) and polyaniline (PANI) [14]; (iv) composite materials. Some of the metal oxide like ruthenium oxides have been widely used in electrochemical capacitors because of the high specific capacitance and excellent electrochemical properties, but their high cost has limited the application on a commercial scale [15]. Other metal oxides have been used as electrode materials because of their pseudocapacitive nature, namely nickel oxide, cobalt oxide, and manganese oxide [3], but these are mostly obtained by chemical methods. ZnO is a promising candidate as an electrode material because of its excellent properties and environmental friendliness. It can be synthesized from agricultural waste using green chemistry. Green chemistry, also known as sustainable chemistry, is the design of chemical products and processes that minimize or eliminate the generation and use of hazardous substances across their entire lifecycle. It focuses on waste prevention, energy efficiency, non-toxic reagents, and the use of renewable feedstocks.

Agricultural wastes are derived from biomass and are often improperly disposed of, thereby constituting a nuisance in the environment. Common agricultural waste includes rice husk, plantain peel, banana peel, rice straw, potato peel, cassava peel, and others; these are usually generated in large quantities and are most often treated by uncontrolled combustion, which causes environmental pollution. Such agricultural waste can be converted into useful and value-added functional material relevant to energy storage systems and bioremediation [16,17]. Ref. [18] reported that green synthesis technology is used to obtain most transition metal oxide nanoparticles. Some of them include nickel oxide (NiO), zinc oxide (ZnO), copper oxide (CuO), iron oxide (Fe_2O_3), cobalt oxide (Co_3O_4), titanium oxide (TiO_2), and manganese oxide (Mn_3O_4). Zinc oxide/activated carbon nanocomposites have been reported in the literature. For example, ref. [15] prepared nanostructured ZnO by a facile microwave method and obtained composite electrodes with activated carbon. In another study, ref. [19] synthesized zinc oxide (ZnO) nanoparticles (NPs) at room temperature using a co-precipitation method for use as an electrode material by forming a composite with activated charcoal (AC) powder used in electrochemical capacitors. Using a green synthesis technique, ref. [20] prepared zinc oxide nanoparticles from Hyptis leaf extract, together with an activated-carbon-based zinc oxide composite, for supercapacitor applications. In another study, a one-step hydrothermal technique was adopted by Mohamed et al. [21] to synthesize ZnO/AC to study its electrochemical performance in the presence of two electrolytes, KOH and H_2SO_4 and an improved performance was recorded. Carbon electrodes can be obtained from biomass, and the properties of the electrode depend on the nature of the biomass and preparation techniques [22]. Most activated carbons are prepared from coconut shell, banana peel, cotton stalk, sugar cane pulp, corn cob, human hair, date seed, cherry seed, leaves, peanut shell, and mulberry trees [23,24]. Agricultural residue-

derived carbons rich in N and O have been shown to achieve specific capacitances beyond 300 F g^{-1} with excellent stability over 5000 cycles [11]. For example, activated carbon was prepared from pomegranate peel waste and was doped with nitrogen and ZnO nanoparticles to synthesize a composite electrode, which demonstrated a specific capacitance of 262 F g^{-1} and 86% capacitance retention at the end of 5000 cycles [25]. In another study, activated carbon was produced from sugarcane bagasse and was decorated with ZnO [26]. Ref. [27] studied the green synthesis and electroanalytical characterization of *Ocimum basilicum*-functionalized ZnO nanoparticles for supercapacitor electrode applications and obtained specific capacitances of 81.12 F g^{-1} in H_2SO_4, 52.24 F g^{-1} in Na_2SO_4, and 21.61 F g^{-1} in KOH at scan rate of 10 mV/s and GCD value of 203.04 F g^{-1} in (H_2SO_4), 84.25 F g^{-1} in (Na_2SO_4), and 41.36 F g^{-1} in (KOH), at 0.02 A g^{-1} respectively. Activated carbon was produced by [28] from Abelmoschus esculentus (AE) seed biomass and formed a composite with Fe_3O_4 as an electrode material to enhance the electrochemical performance of supercapacitors. They obtained specific capacitances of 119.97 F/g for AE-AC and 205.86 F g^{-1} for AEAC-doped Fe_3O_4 at 0.05 A g^{-1}, respectively. In another study, ref. [29] demonstrated the fabrication of $ZnMn_2O_4$-CNT nanocomposites using acid-modified MWCNTs and a one-step green hydrothermal method for supercapacitor application. They observed that the synergistic interaction between the MWCNTs and the $ZnMn_2O_4$ nanoparticles contributed to the specific capacitance of 103 Fg^{-1} of the as-fabricated electrode.

The cost of electrodes and consequently that of supercapacitors are reduced by fabricating them from biomass because they are scalable, cheap, readily available, and cost-effective [30,31]. By incorporating AC, an EDLC material, into a pseudocapacitive material (metal oxides/transition metal oxides), effective active sites, a larger electrode/electrolyte interfacial area and faster transfer of active ions can be achieved which promotes electrochemical reaction and a highly efficient electrocatalysts [32,33]. Therefore, developing composite electrode material of transition metal oxides nanoparticles from biomass with carbon is promising and of great potential in enhancing the electrical conductivity, specific surface area, electro-active sites, and chemical stability while also reduces possible aggregation of metal oxide nanoparticles [34,35]. The porous carbon, as a composite with the metal oxide also provides EDLC charge storage and support for the metal oxide nanoparticles thereby improving an effective specific surface area, good electric conductivity, and wettability of the active materials by the electrolyte. Also, the transfer of electrolyte ions and proper utilization of pseudocapacitive active materials are ensured even at high rates of charging and discharging, leading to better performance and cycle stability [33,36–38]. In another study [39], the electrochemical performance of 1,4-benzene diboronic acid (DBA) and AC composite (DBA-AC) as an active material for supercapacitors was reported. The optimized DBA-AC electrode had a specific capacitance of 211.4 F g^{-1} at 20 mV s^{-1} as a result of the large surface area and sufficient functional groups.

Using the hydrothermal method, the preparation and characterization of a high-performance Fe_3O_4/RGO anode for supercapacitors was investigated by [40]. They obtained a high specific capacitance of 571.2 F g^{-1} at a current density of 1 A g^{-1} for the Fe_3O_4/rGO composite and 214.7 F g^{-1} for pure Fe_3O_4. A novel energy storage system with hierarchical porous activated carbon and redox-active organic materials as an active hybrid cathode material for Zinc-ion hybrid supercapacitors (ZIHSCs) was developed by [41]. The fabricated device exhibited an outstanding energy output of 250 Wh kg^{-1} at a current density of 0.1 A g^{-1} and a power output of 9.5 kW kg^{-1} at a current density of 10 A g^{-1}, respectively. In another study [42] produced graphitic carbon nitride (GCN) material from urea and hydrothermally doped it with fluorine atoms (F-doped GCN) as an electrode material for supercapacitors. The specific capacitance of the GCN and F-doped GCN supercapacitors was calculated as 39.75 F g^{-1} and 305.72 F g^{-1} at a frequency of 0.01 Hz. In another study, ref. [28] produced activated carbon from Abelmoschus esculentus (AE) seed biomass and formed a composite with Fe_3O_4 as electrode material to enhance the electrochemical performance of supercapacitors. They obtained specific capacitances of 119.97 F/g for AE-AC and 205.86 Fg^{-1} for AEAC-doped Fe_3O_4 at 0.05 A g^{-1} respectively.

Although transition metal oxide and carbonaceous composite electrodes have attracted widespread interest for high-performance supercapacitors, conventional synthetic pathways frequently rely on non-renewable fossil fuel-derived carbon precursors, toxic reducing agents, and hazardous organic solvents. Furthermore, high-capacitance metal-based oxides pose significant environmental hazards, supply-chain risks, and economic toxicity.

To resolve the trade-off between high electrochemical performance and environmental sustainability, this work presents a green chemistry-driven pathway for the fabrication of a zinc oxide–activated carbon nanocomposite electrode from agricultural waste.

In this study, we investigated the synergistic potential of electrode materials formed from activated carbon (AC) obtained from unripe plantain peel, an agricultural waste, by carbonization and activation, and zinc oxide nanoparticles prepared using an agricultural waste-derived silica-rich material (rice husk) as a resource, reducing waste and potentially lowering the environmental burden associated with conventional ZnO synthesis. We developed four AC-ZnO nanocomposites with different ZnO loadings. This study is limited to investigating

electrode material performance from the aforementioned precursors and does not extend to device fabrication, which will be considered in a further study. The ZnO-AC composites were used as the electroactive material coated on a nickel foam current collector to optimize electrochemical performance in 6 M KOH electrolyte in a three-electrode configuration using cyclic voltammetry, galvanostatic charge–discharge, and electrochemical impedance spectroscopy on a Bio-Logic potentiostat (BioLogic Science Instruments SAS, Seyssinet-Pariset, France).

Electrode material from this agricultural waste is justified because it combines waste valorization with functional electrochemical properties, producing a hybrid electrode that balances the performance of supercapacitor electrode material such as specific capacitance, and sustainability.

This study also contributes to the volume of information and knowledge on agricultural-waste valorization, resource recovery, and use of a biomass-derived inorganic matrix in the application of electrode material for energy storage systems. It also emphasizes the sustainability and utilization of waste-to-energy systems (wealth), thereby combating environmental nuisance from such agricultural waste.

2. Experimental Procedure

The synthesis of zinc oxide nanoparticles from the rice husk route started with the controlled combustion of dried rice husks in a muffle furnace at an optimized temperature of 637 °C and 4.8 h, producing white rice husk ash (RHA) rich in silica (SiO_2). To extract silica, the RHA was mixed with 1 M sodium hydroxide (NaOH) and heated to 90 °C for 1.5 h under continuous stirring with a magnetic stirrer. This process dissolves the silica, converting it into sodium silicate. The mixture was filtered to remove any unreacted residues, and a clear sodium silicate solution was obtained. To precipitate silica gel, 1M hydrochloric acid (HCl) was added dropwise to the sodium silicate solution while stirring until the pH reached 7–8, resulting in the formation of silica gel. The gel was washed five times with distilled water to remove residual sodium ions and dried at 110 °C.

For the synthesis of ZnO nanoparticles, a zinc precursor solution was prepared by dissolving 1.171 M zinc acetate ($ZnC_4H_6O_4$) in distilled water to obtain a clear solution. The dried silica gel from the previous step was added to the zinc acetate solution, where it served as a template and stabilizer for nanoparticle formation. The pH of the mixture was adjusted to 10 using the base NaOH to initiate the formation of ZnO nanoparticles. The mixture was heated at 81.78 °C for 1.5 h under constant stirring, leading to the formation of a suspension containing ZnO nanoparticles. After cooling, the nanoparticles were collected by filtration, then washed five times with distilled water to remove any residual ions. Finally, the product was dried at 110 °C and calcined at optimized condition of 588 °C for 1.5 h to enhance crystallinity and eliminate any remaining organic impurities, resulting in the formation of ZnO nanoparticles. The mechanism involved is

$$\text{Rice husk (controlled combustion)} \rightarrow SiO_z\text{-rich RHA} \tag{1}$$

Dissolution of zinc acetate, that is dispersion of the zinc precursor gives

$$Zv(CH_3COO)_2 \rightarrow Zn^2 + 2CH_3COO^- \tag{2}$$

The Zn^2 ions become available for subsequent hydroxide precipitation. The addition of sodium hydroxides will lead to the formation of zinc hydroxide as follows:

$$NaOH \rightarrow Na^+ + OH^- \tag{3}$$

$$Zn^2 + 2OH^- \rightarrow Zn(OH)_2 \tag{4}$$

In strong alkaline condition, soluble zincate hydroxide complexes can be formed.

$$Zn(OH)_2 + 2OH^- \rightleftarrows [Zn(OH)_2]^{2-} \tag{5}$$

RHA contains surface silanol group ≡Si–OH and deprotonated siloxide sites: ≡Si–O^-. These oxygen-containing surface sites can interact with Zn^{2+} or zinc-hydroxo species. Consequently, RHA may act as a heterogeneous nucleation surface. Conceptually, ≡Si–O^- + Zn^{2+} ≡Si–O–Zn^{2+} followed by further condensation and Zn-O formation.

During calcination, the precipitated zinc hydroxide precursor will be thermally decomposed as

$$Zn(OH)_2(s) \rightarrow ZnO(s) + H_2O(g) \tag{6}$$

ZnO synthesized under optimized conditions of 588 °C and 1.5 h yielded 38 g of product and was subsequently used in the fabrication of the ZnO-AC composite electrode. From an energy perspective, the theoretical electrical demand of the calcination step was estimated from the nominal furnace power using (E = Pt)

where E is energy (kWh), P is furnace power (kW), and t is time (h). For a furnace rated at 1.2 kW and operated for 1.5 h, the estimated electrical energy requirement was 1.8 kWh per batch, equivalent to 6.48 MJ. Considering the 38 g ZnO obtained under the optimized condition, this corresponds to a theoretical specific energy requirement of 47.37 kWh kg^{-1} (ZnO) or 170.5 MJ kg^{-1} (ZnO).

This energy assessment provides an additional sustainability perspective on the optimized synthesis route. In particular, the process simultaneously utilizes rice husk ash as an agricultural-waste-derived feedstock and converts it into a value-added ZnO material for electrochemical energy-storage applications. The relatively short calcination duration of 1.5 h limits the duration of thermal processing, while the optimized batch produced a comparatively high ZnO output relative to the fixed furnace energy demand. Thus, the optimized condition represents not only the condition selected on the basis of the design of experiment (DOE) response but also a practical operating point for subsequent electrode fabrication.

It should be noted that the calculated 1.8 kWh represents the theoretical electrical energy demand based on the furnace rating, assuming continuous operation at 1.2 kW. It should therefore not be interpreted as the measured electricity consumption, since actual furnace power draw may vary during heating, temperature stabilization, and thermostatic cycling. Direct measurement using an energy meter would provide a more rigorous energy assessment. Nevertheless, the calculated specific energy requirement provides a useful first-order indicator of the energy intensity associated with the optimized RHA-to-ZnO conversion. The synthesis exhibits sustainability advantages through agricultural-waste valorization, process optimization and relatively short-duration thermal treatment.

Composites of the as-prepared ZnO and the AC from unripe plantain peel were formed in four different ratios, made up of 50% ZnO and 50% AC (1:1), 66.67% ZnO and 33.33% AC (2:1), 75% ZnO and 25% AC (3:1), and 80% ZnO and 20% AC (4:1). The X-ray diffraction (XRD) patterns of the ZnO nanoparticles and of the ZnO-AC composite were recorded using a Rigaku D/max rA X-ray diffractometer (Rigaku Corporation, Akishima-shi, Tokyo, Japan) with a Cu Kα radiation source (λ = 1.5406 Å) at a scanning rate of 2° per minute within a 2θ range of 10–80°. Brunauer–Emmett–Teller (BET) analysis of the ZnO-AC nanocomposites were carried out using absorbate gas nitrogen, outgas time and temperature are 3 h and 250 °C respectively to determine the textural properties.

2.1. Electrode Preparation

Commercial nickel foam substrate (NF), thickness 1.6 mm, was pretreated to eliminate surface organic passivants, native oxides, and surface contaminants prior to active material deposition. Pre-cut NF pieces (1.0 cm × 2.0 cm) were degreased in absolute acetone under ultrasonication for 15 min to remove hydrophobic grease and industrial lubricants. To eliminate native nickel oxide (NiO) layers and expose active metallic nickel sites, the substrate was acid-etched in a 2 M HCl aqueous solution for 10 min. The etched NF was subsequently thoroughly washed with deionized water until neutral pH 7. It was rinsed with absolute ethanol. Finally, the cleaned NF was dried in an oven at 60 °C for 12 h.

ZnO nanoparticles were mixed with activated carbon in four different ratios (1:1, 2:1, 3:1 and 4:1) by physical mixing. The ZnO powder and activated carbon that formed the composite were weighed in the desired ratio and mixed using a mortar and pestle for 1 h at 25 °C to ensure intimate contact (homogeneity) between the two phases. A paste was prepared by mixing 80% active electrode material (ZnO-AC composites), 10% carbon black and 10% polyvinylidene fluoride binder, dispersed in N-methyl-2-pyrrolidone. The paste was applied with a brush on a 1.0 cm × 1.0 cm active region of the pre-weighed nickel foam current collector and dried at 25 °C.

The mass load of 5.618 g cm^{-2} ZnO-AC composite (active material), standard deviation 5.618 ± 0.005 g cm^{-2} (mean ± SD, n = 4), was determined and used in the calculation of material performance from CV and GCD.

2.2. Electrochemical Characterization of Electrode Material

The electrochemical performance was evaluated in a conventional three-electrode system (half-cell) equipped with an Ag/AgCl (3 M KCl) reference electrode, a graphite rod as the counter electrode, and the AC–ZnO nanocomposite as the working electrode. The measurements were performed at room temperature using cyclic voltammetry (CV), galvanostatic cycling at voltage window is from −0.4 to 0.4 (i.e. 0.8V), with potential limitation (GCPL) and electrochemical impedance spectroscopy (EIS) at frequencies range of 100 kHz–10 mHz. The testing was carried out using a computer-controlled multi-channel Bio-Logic VMP3 potentiostat/galvanostat driven by EC-Lab® v10.40 software. Electrode performance parameters were calculated from CV and GCD profiles.

3. Results and Discussion

3.1. Structural Analysis

X-ray diffraction analysis characterized the crystal structure of the prepared ZnO and ZnO-AC composites. Figures 1 and 2 show the XRD patterns of the as-prepared ZnO and the ZnO-AC composites. In Figure 1, the ZnO diffraction pattern shows well-defined, sharp peaks, indicating a highly crystalline material. The major diffraction peak observed at $2\theta \approx 36.98°$ corresponds to the (101) crystallographic plane of hexagonal wurtzite ZnO, but is slightly shifted from the standard 36.25°. According to JCPDS Card No. 36-1451, Additional diffraction peaks observed around 66.78° and 74.56° can be indexed to the (200) and (004) planes, respectively, since they are closer to the standard with a defect shift. This further confirms the formation of the hexagonal ZnO crystal structure. In Figure 2, the XRD patterns of the ZnO-AC composites with ZnO-AC ratios of 1:1, 2:1, 3:1, and 4:1 exhibited the characteristic reflections of hexagonal wurtzite ZnO. The major reflections are indexed to the (100), (002), (101), (102), (110), (103), (200) and (112) planes at approximately 31.76°, 34.42°, 36.25°, 47.53°, 56.60°, 62.86°, 66.37° and 69.09° respectively, in agreement with JCPDS/PDF No. 36-1451. The persistence of these reflections across all compositions confirmed that incorporation of biomass-derived activated carbon does not alter the fundamental wurtzite ZnO crystal structure. The broad diffuse scattering contribution is attributable to the poorly crystalline carbonaceous component of the activated carbon. Although the rice-husk origin of the ZnO precursor makes residual silica chemically plausible, no characteristic set of crystalline SiO_2 reflections can be unequivocally identified. Therefore, crystalline silica cannot be assigned as a secondary phase solely from the present XRD patterns. Likewise, no additional diffraction sequence provides conclusive evidence for Zn_2SiO_4 or $Zn(OH)_2$. The pronounced (002) reflection at approximately 34.4° indicates a preferential crystallographic orientation associated with the c-axis of hexagonal wurtzite ZnO. The observed variations in peak intensity are therefore more appropriately associated with changes in ZnO-AC composition, crystallinity, preferred orientation, and interaction between the ZnO crystallites and carbon matrix rather than formation of a new crystalline ZnO phase.

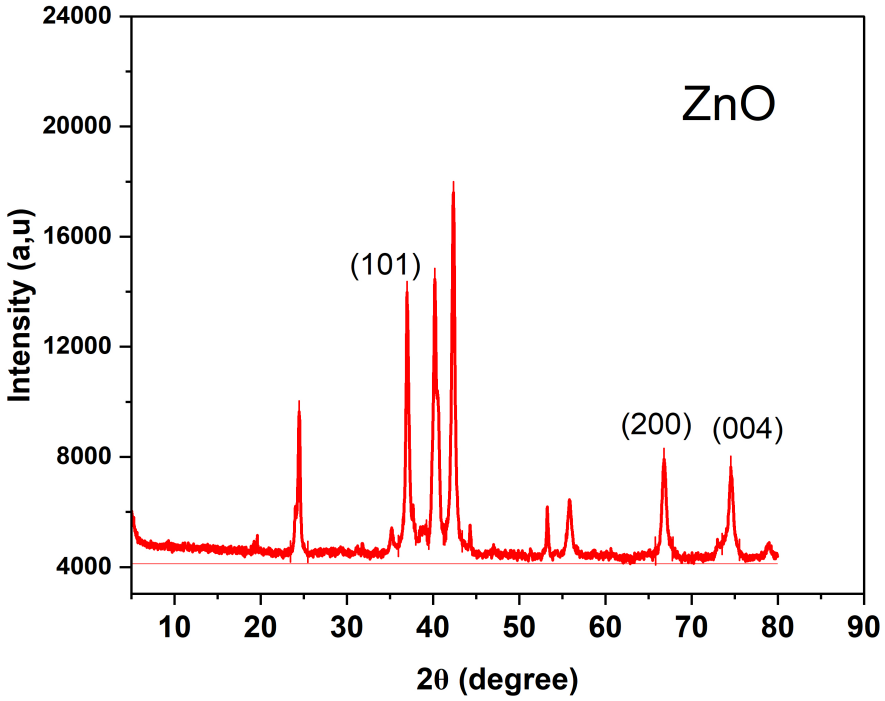


Figure 1. XRD pattern of ZnO nanoparticle.

The SEM micrographs of the ZnO/AC (1:1) composite in Figure 3 revealed a heterogeneous, highly textured morphology comprising irregularly shaped aggregates surrounded by finer particulate domains. At the lower magnification (20 μm scale), the composite exhibited a hierarchical arrangement characterized by relatively large agglomerates embedded within a matrix of smaller particles, indicating substantial morphological heterogeneity. Increasing the magnification to the 10 μm scale revealed a substantially rougher and more finely textured surface, with numerous fine particulate features distributed across the larger aggregates. Such surface characteristics are favorable for electrochemical applications because they help to increase the number of accessible solid– electrolyte accessibility and limit the effective utilization of ZnO sites.

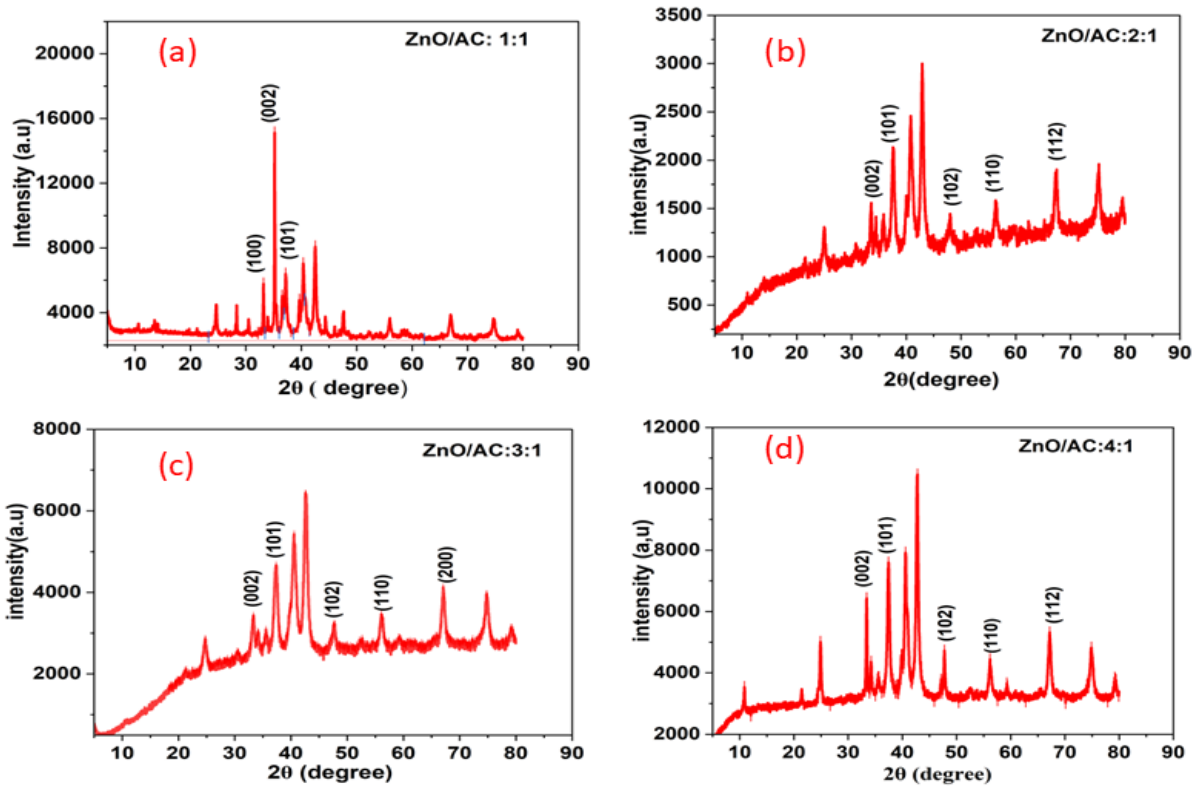


Figure 2. XRD pattern of ZnO/AC nanocomposites (**a**) ratio 1:1 (**b**) ratio 2:1 (**c**) ratio 3:1 and (**d**) ratio 4:1.

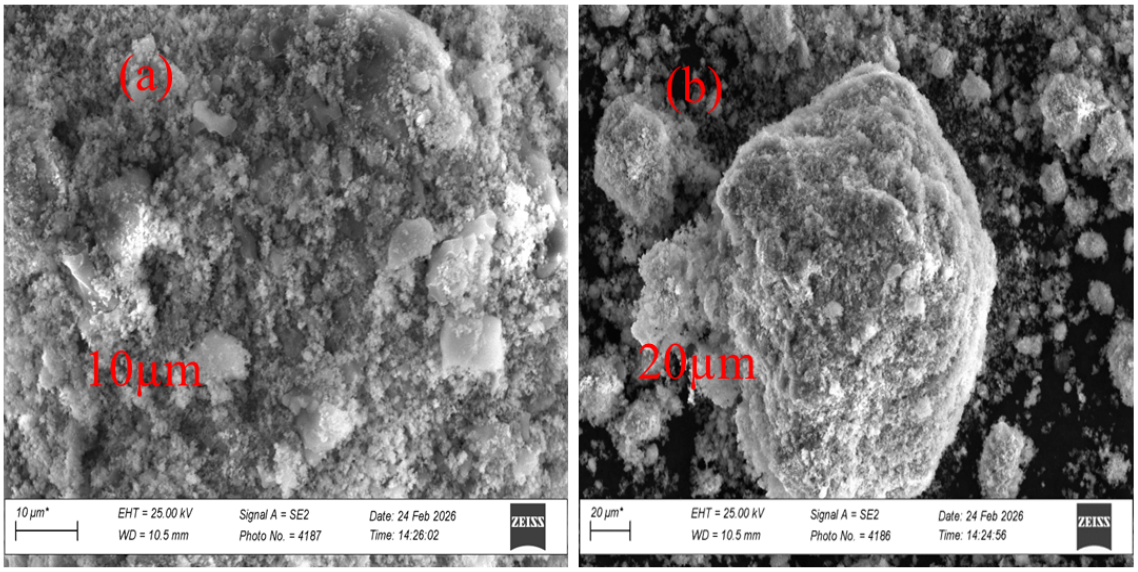


Figure 3. SEM (Cambridge Scientific Instrument Company, Cambridge, UK) image of ZnO/AC 1:1 nanocomposite at (**a**) 10 µm magnification and (**b**) 20 µm scale.

The SEM micrographs of the ZnO/AC (2:1) nanocomposite in Figure 4 revealed a heterogeneous hierarchical morphology characterized by irregularly shaped aggregates, densely packed particulate domains, and a highly corrugated surface. At the lower magnification, the material exhibited relatively large interconnected agglomerates, whereas the higher-magnification micrograph resolved a finer granular architecture comprising ZnO-rich particulate features distributed over the carbonaceous matrix. The coexistence of compact domains and interparticle voids indicated that the composite formation resulted in substantial interfacial contact between ZnO and activated carbon, but also produced a degree of particle aggregation.

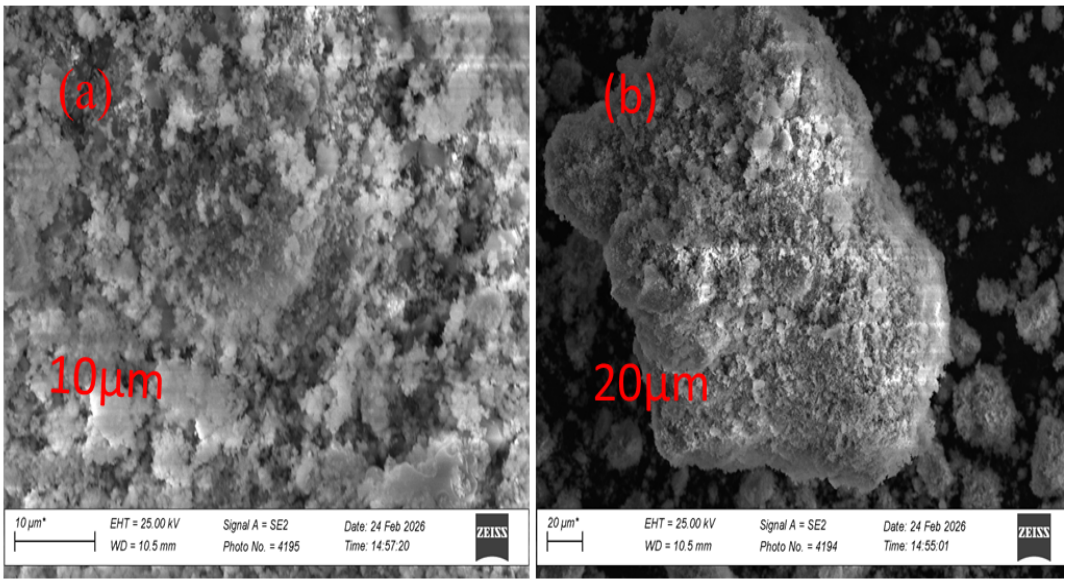


Figure 4. SEM image of ZnO/AC 2:1 nanocomposite at (**a**) 10 µm and (**b**) 20 µm scale.

Figure 5 shows SEM micrographs of the ZnO/AC (3:1) nanocomposite, revealing a highly heterogeneous, strongly aggregated architecture. At the 20 µm scale, a large irregular agglomerate dominates, surrounded by numerous smaller particulate clusters. The surface of the principal aggregate is highly corrugated and exhibits a cauliflower-like texture, indicating extensive secondary aggregation of fine particles. At higher magnification (10 µm), the surface is composed of densely packed fine particulate features with localized compact domains and relatively narrow interparticle voids.

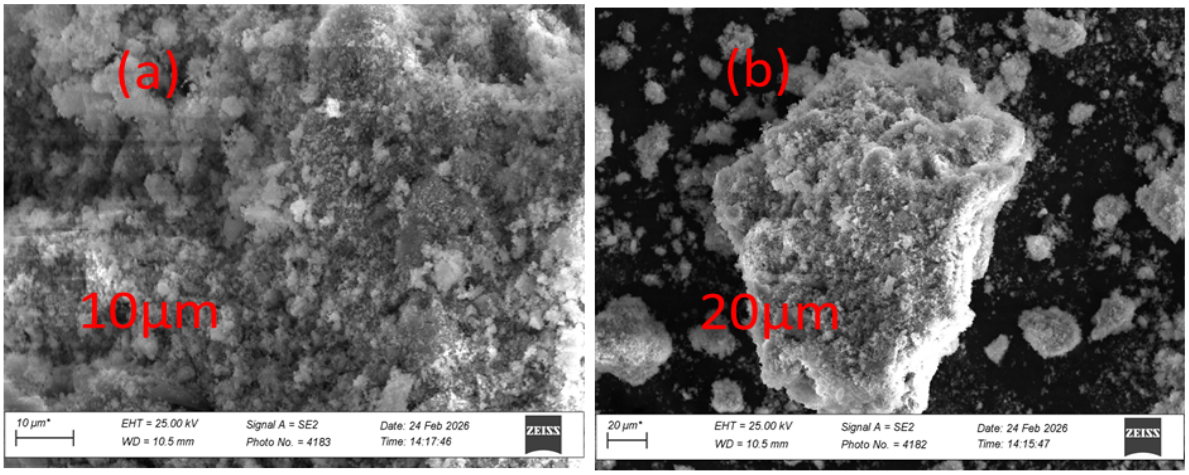


Figure 5. SEM image of ZnO/AC 3:1 nanocomposite at (**a**) 10 µm and (**b**) 20 µm scale.

The SEM micrographs of the ZnO/AC (4:1) nanocomposite show a hierarchical agglomerated morphology, with fine ZnO-rich particulate domains assembled into larger secondary aggregates on the activated-carbon matrix, as shown in Figure 6. The rough and highly textured surface, together with the interparticle voids observed at higher magnification, is expected to promote electrolyte wetting and provide short-range ion-transport pathways. Nevertheless, the pronounced aggregation associated with the relatively high ZnO content may partially shield the carbon surface and obstruct a fraction of the underlying porous network, thereby reducing the effective electrochemically accessible surface area.

The textural characteristics of the ZnO/AC nanocomposites demonstrate a strong dependence on composition, with the ZnO/AC ratio substantially modifying the accessible surface area and pore volume while maintaining a relatively constant average pore diameter (2.92–3.02 nm) as could be seen in Table 1. Pristine AC exhibited the highest surface area (970.805 m^2 g^{-1}) and pore volume (0.863 cm^3 g^{-1}), confirming its highly developed porous structure. Incorporation of ZnO with surface area 246 m^2/g progressively alters this architecture of the composite.

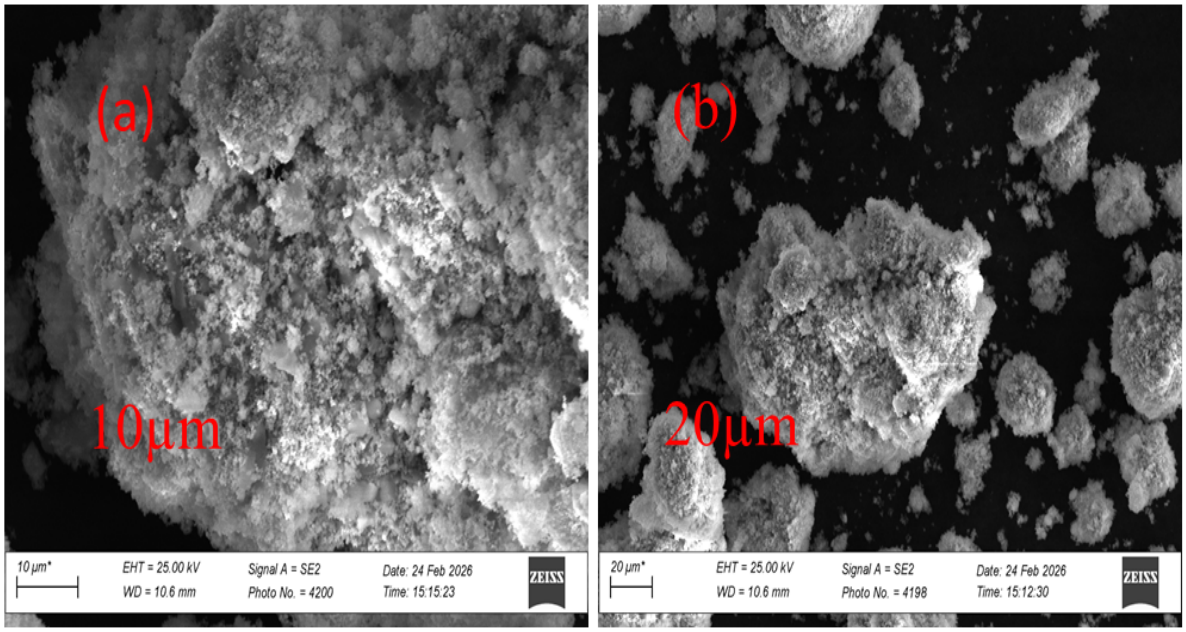


Figure 6. SEM image of ZnO/AC 4:1 nanocomposite at (**a**) 10 µm and (**b**) 20 µm scale.

Table 1. Summary of BET results for the ZnO-AC nanocomposites and AC.

ZnO/AC Ratio	Surface Area (m^2/g)	Pore Volume (cm^3/g)	Pore Diameter (nm)
1:1	221.643	0.202	2.94
2:1	659.556	0.582	3.02
3:1	188.404	0.171	2.92
4:1	380.075	0.335	3.00
AC	970.805	0.863	3.00
ZnO	246	0.174	2.14

The DFT and DA pore-size distributions shown in Figures 7 and 8, respectively, revealed that both pristine AC and ZnO-AC nanocomposites possess predominantly large-micropore/small-mesopore populations, with pore widths concentrated approximately between 1.8 and 2.8 nm. The pristine AC exhibited the highest differential pore-volume contribution, whereas incorporation of ZnO substantially modified the pore architecture of the carbon matrix. Among the composites, ZnO-AC-2:1 displayed the most pronounced pore-volume distribution, particularly within the 2.2–2.8 nm region, which is consistent with its high BET surface area of 659.6 $m^2\ g^{-1}$. Nevertheless, its superior textural porosity does not translate into the highest electrochemical specific capacitance. The ZnO-AC-1:1 exhibited substantially higher specific capacitance despite possessing a considerably lower BET surface area of 221.6 $m^2\ g^{-1}$. This divergence demonstrated that total textural surface area and pore volume alone are insufficient descriptors of electrochemical performance. Rather, the accessibility and connectivity of pores to electrolyte ions, pore–ion size matching, electronic conductivity and the electrochemically active ZnO-AC interface collectively determine the effective charge-storage capacity. The pores near and below 2 nm can provide high-density sites for electric-double-layer formation, whereas the small mesopores above 2 nm facilitate electrolyte transport toward these sites. The better performance of the 1:1 composite therefore suggests a more favorable balance between accessible carbon surface, ZnO electroactive sites, ionic transport and electronic conduction.

In contrast, the higher ZnO content in the 2:1 composite may increase the nominal textural porosity while simultaneously promoting partial pore blocking, increased diffusion tortuosity and/or disruption of the conductive carbon network, thereby limiting effective utilization of the available surface during electrochemical cycling. These results emphasized that optimizing ZnO/AC electrodes requires control of pore accessibility and interfacial architecture rather than maximizing BET surface area alone.

In general, the DFT analysis indicated that the electrochemical advantage of ZnO-AC-1:1 originated not from maximum pore volume but from an optimized pore–electrolyte–interface relationship in which sufficiently large pores facilitate ion transport while accessible ZnO-AC interfaces provided efficient charge-storage sites.

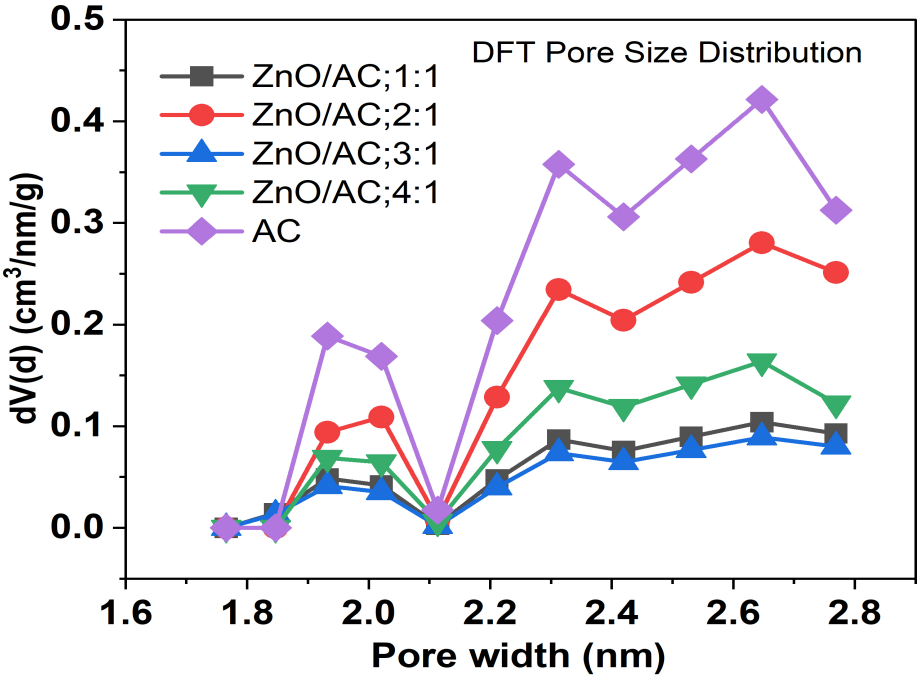


Figure 7. Pore size distribution of nanocomposite material by DFT/NLDFT method.

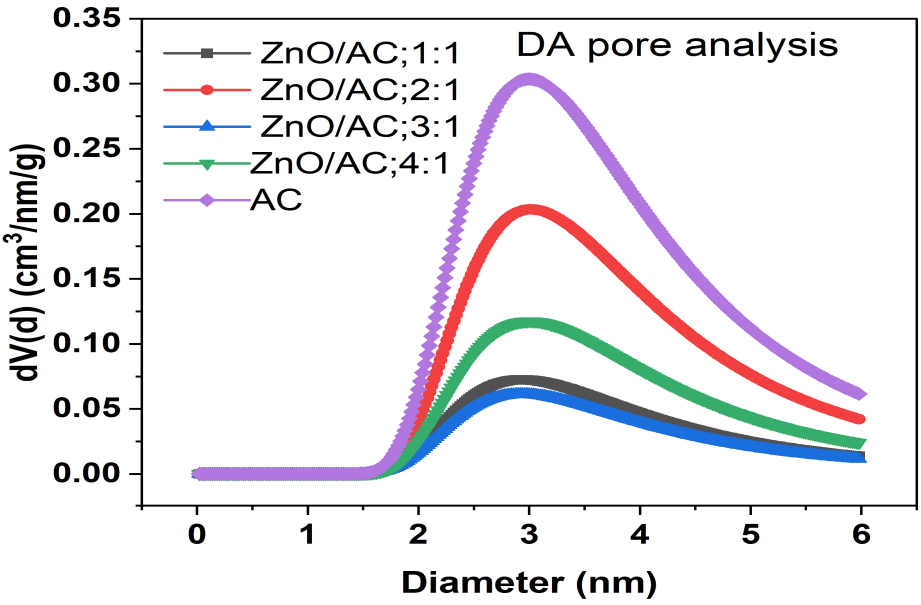


Figure 8. Pore size distribution of nanocomposite material by DA method.

3.2. Electrochemical Performance of Nanocomposite Electrodes

3.2.1. Electrochemical Charge Storage Kinetics and Rate Capability Analysis

To evaluate the charge storage mechanism and practical rate capability of the synthesized ZnO-AC nanocomposites as potential electrode materials for supercapacitors, cyclic voltammetry (CV) measurements were conducted across a wide range of scan rates (5 to 100 mV s^{-1}) in 6 M KOH electrolyte within a potential 0.8 V, and reference electrode Ag/AgCL, Figure 9a–d displays the characteristic CV profiles, where the synergistic combination of electric double-layer capacitive (EDLC) behavior from the porous activated carbon (AC) framework and faradaic redox transitions from the zinc oxide (ZnO) nanoparticles is evident. The specific capacitance was calculated from the measurement results of CV according to Equation (7).

$$C_{sp} = \int I(V)dV / 2mv(\Delta V) \quad (7)$$

where C_{sp} is specific capacitance (F g^{-1}), m is the mass of the electroactive material of the electrode (g), I is the discharge current (A), dt is the discharge time (s), ΔV is the voltage window, and ν is the scan rate (Vs^{-1}).

To quantitatively differentiate between surface-controlled capacitive processes (EDLC and surface pseudo capacitance) and bulk diffusion-controlled intercalation processes, the dependence of peak current (i_p) on sweep rate (v) was analyzed using the empirical power-law relationship as

$$i_p = a \cdot v^b \tag{8}$$

Taking the logarithmic transformation yields

$$\log(i_p) = b \cdot \log(v) + \log(a) \tag{9}$$

where b is the characteristic kinetic exponent determined from the slope of $\log(i_p)$ versus log(v) (Figure 10). Standard electrochemical theory dictates that a b-value of 0.5 represents a sluggish, semi-infinite diffusion-controlled faradaic reaction typical of battery-like materials, whereas a b-value of 1.0 designates a rapid, surface-controlled capacitive process. Intermediate values (0.5 < b < 1.0) indicate mixed kinetic behavior.

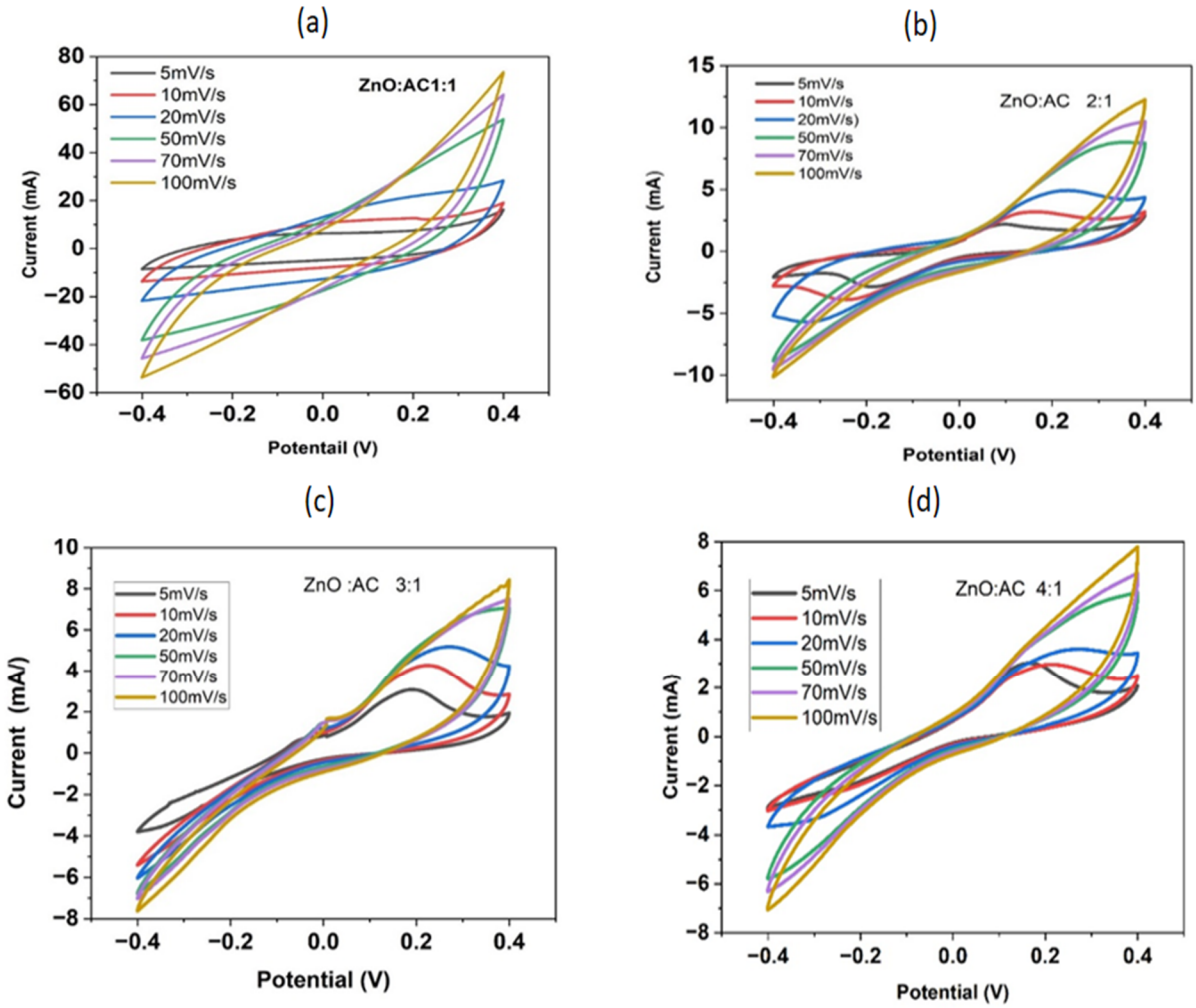


Figure 9. Cyclic voltammetry (CV) profiles of the ZnO/AC nanocomposites with the following ratios: (**a**) 1:1 (**b**) 2:1 (**c**) 3:1, and (**d**) 4:1.

As summarized in Table 2, the kinetic exponent b exhibited a strong compositional sensitivity to the ZnO:AC mass ratio. For the ZnO-AC 1:1 composite, the anodic and cathodic b-values were calculated to be 0.55282 and 0.62098, respectively (b_{avg} = 0.58690). This confirms a balanced hybrid charge-storage mechanism where the porous carbon network provides accessible channels for rapid surface ion electro-sorption, while embedded ZnO nanoparticles participate in surface-confined pseudocapacitive redox processes. Increasing the ZnO content to ZnO-AC 2:1 shifted b_a to 0.52540 and b_c to 0.56616, shifting the charge storage mechanism closer to purely diffusion-controlled faradaic kinetics (b → 0.50).

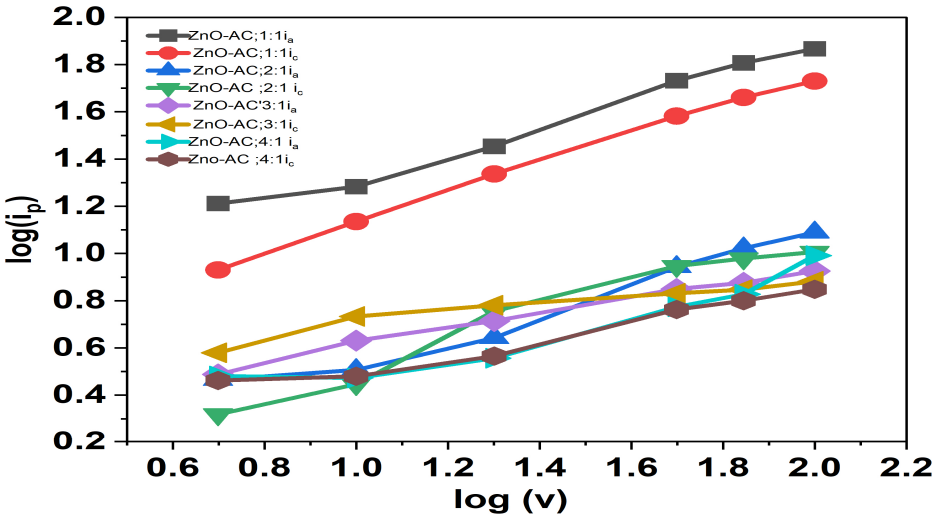


Figure 10. $\log(i_p)$ vs log (v) plots for b-value determination.

Table 2. Anodic and cathodic b-values derived from power-law fitting log (i) vs log (v) for ZnO-AC nanocomposites at varying mass ratios.

Composite Material	Anodic b-Value (b_a)	Cathodic b-Value (b_c)	Average b-Value (b-{avg})	Dominant Kinetic Regime
ZnO-AC 1:1	0.55282	0.62098	0.58690	Hybrid Diffusion–Capacitive
ZnO-AC 2:1	0.52540	0.56616	0.54578	Semi-Infinite Diffusion Dominated
ZnO-AC 3:1	0.32713	0.20403	0.26558	Mass-Transport/Ohmic Limited (b < 0.5)
ZnO-AC 4:1	0.35029	0.32721	0.33875	Mass-Transport/Ohmic Limited (b < 0.5$)

Crucially, higher metal oxide loadings (ZnO/AC 3:1 and 4:1) result in an anomalous decay of b-values below the theoretical lower boundary of 0.5 (b_c dropping to 0.20403 for 3:1 and 0.32721 for 4:1). In solid-state electrochemistry, sub-theoretical exponents (b < 0.5) indicate severe kinetic bottlenecking caused by uncompensated internal resistance (iR drop), loss of electronic percolation pathways, and diffusion starvation within deep particle agglomerates. As pure ZnO possesses intrinsic semiconducting properties with low electronic conductivity, excessive loading disrupts the conductive carbon network, transforming the composite into an ohmically restricted matrix.

3.2.2. Scan Rate-Dependent Specific Capacitance and Rate Capability

The practical impact of these kinetic regimes was further investigated by calculating the gravimetric specific capacitance (C_{sp}) across sweep rates ranging from 5 to 100 mV s^{-1}. As shown in Table 3 and Figure 11, all nanocomposite formulations demonstrate an inverse relationship between specific capacitance and scan rate. At low sweep rates (5 mV s^{-1}), electrolyte ions (K+/OH−) have sufficient diffusion time to traverse the porous electrode structure and engage both the outer surface and the inner electroactive ZnO sites. As the scan rate increases to 100 mV s^{-1}, the shortened diffusion time limits charge storage primarily to fast, outer-surface double-layer adsorption, causing a drop in C_{sp}.

The ZnO-AC 1:1 nanocomposite demonstrated superior capacitive performance across all testing conditions, achieving an impressive maximum specific capacitance of 322.0 F g^{-1} at 5 mV s^{-1}. This performance is nearly 3× higher than the 2:1 nanocomposite (113.0 F g^{-1}) and nearly 8× higher than the 3:1 (46.7 F g^{-1}) and 4:1 (40.7 F g^{-1}) nanocomposites. Furthermore, the 1:1 formulation maintained superior rate capability, retaining 39.8 F g^{-1} (12.36% retention) at 100 mV s^{-1}, whereas the 4:1 composite retained a negligible 1.80 F g^{-1} (4.42% retention). The anomaly observed at 20 mV s^{-1} for the 3:1 composite can be attributed to severe localized ion starvation and transient polarization effects within the highly resistive electrode.

Table 3. Gravimetric specific capacitance (C_{sp}, F g^{-1}) of ZnO-AC electrode materials as a function of CV scan rate (5–100 mV s^{-1}).

Scan Rate (mV s^{-1})	Specific Capacitance (F g^{-1}) Electrodes Materials			
	ZnO:AC: 1:1	ZnO:AC 2:1	ZnO:AC: 3:1	ZnO:AC 4:1
5	322	113	46.7	40.7
10	246	40.7	29.6	23.5
20	179	28.2	1.75	15.0
50	90.7	12.2	7.89	7.59
70	63	8.43	5.64	5.49
100	39.8	5.9	4.01	1.80
Retention (5 → 100 (mV s^{-1})	12.36%	5.22%	8.59%	4.42%

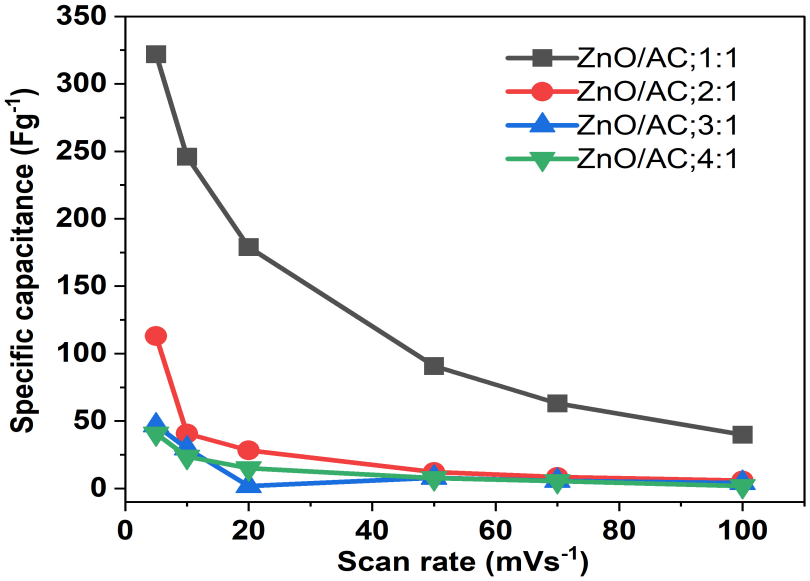


Figure 11. Specific capacitance as a function of scan rate for ZnO-AC nanocomposites.

3.2.3. Mechanistic Correlation: Kinetics vs Performance

Correlating the power-law kinetic parameters (Table 2) directly with the gravimetric capacitance data (Table 3) reveals the overarching structure-property-performance relationships governing these nanocomposites.

Conductive Percolation vs Electroactive Site Balance: In the 1:1 composition, activated carbon forms a continuous, three-dimensionally interconnected conductive framework that wraps around the ZnO nanoparticles. This architecture ensures low charge transfer resistance (Rct) while providing a high surface area for rapid EDLC charging. Simultaneously, the accessible ZnO centers undergo faradaic redox reactions, establishing the hybrid kinetic exponent (b_{avg} = 0.587) and high capacitance (322 Fg^{-1}).

Diffusion Limitations in Metal-Oxide Rich Systems: In the 2:1 composition, the increased proportion of ZnO shifts kinetics toward semi-infinite diffusion control (b_{avg} = 0.546). and as solid-state diffusion is intrinsically slower than electric double-layer charging. C_{sp} drops by 64.9% at 5 mV s^{-1} relative to the 1:1 sample, with rapid specific capacitance fade as scan rates increase.

Pore Clogging and Ohmic Polarization (b < 0.5): At excessive metal oxide ratios (3:1 and 4:1), ZnO nanoparticles aggregate into dense clusters that block the micro- and mesopores of the activated carbon matrix. This structural blockage restricts ion transport channels and disrupts electronic percolation. The resulting high equivalent series resistance (ESR) prevents electrolyte ions from reaching inner active sites even at slow scan rates (5 mV s^{-1}), resulting in low specific capacitance (40.7–46.7 F g^{-1}) and low kinetic exponents (b < 0.5).

Consequently, the 1:1 mass ratio of ZnO:AC represents the optimal compositional threshold, providing the rapid kinetics and rate capability required for better performance in supercapacitor applications.

3.2.4. Galvanostatic Charge-Discharge (GCD) Evaluation and Comprehensive Parameter Correlation

To complement the cyclic voltammetry measurements and further quantify charge storage performance under steady-state operational conditions, galvanostatic charge-discharge (GCD) tests were executed across current densities ranging from 1 to 10 A g^{-1}, the profile is shown in Figure 12. The specific capacitance values calculated

from the discharge curves by considering the iR drop according to Equation (10) are presented in Table 4 and Figure 13 is the comparative plot matching C_{sp} (GCD) with b-value kinetics.

$$C_{sp} = {Ixdt}/{mdV} \quad (10)$$

Consistent with the CV scan-rate and power-law kinetic evaluations, the ZnO: AC (1:1) nanocomposite demonstrated exceptional charge storage capability, delivering a maximum gravimetric specific capacitance of 227.56 F g^{-1} at 1 A g^{-1}. In sharp contrast, increasing the Zinc oxide loading to 2:1, 3:1, and 4:1 resulted in a catastrophic drop in performance, yielding low specific capacitance values of 14.97 F g^{-1}, 3.84 F g^{-1}, and 4.30 F g^{-1} at 1 A g^{-1}, respectively.

Correlating these GCD findings with the kinetic exponent (b-value) parameters yields key insights into the underlying charge storage mechanisms; the equation for the b-value is given in Equation (9).

Conductive Matrix Integrity and Kinetic Reversibility ZnO-AC (1:1 Ratio): The high galvanostatic specific capacitance of the 1:1 formulation 227.56 F g^{-1} is directly enabled by its hybrid kinetic mechanism (b_{avg} = 0.587). The 1:1 ratio maintains an optimal conductive carbon network that minimizes equivalent series resistance (ESR), permitting rapid surface pseudocapacitive charge transfer and reversible faradaic redox reactions at the ZnO surface interface.

Ohmic Polarization and Mass Transport Blockage (ZnO-AC ≥ 2:1 ratios): The dramatic 93.4% specific capacitance loss observed when transitioning from 1:1 (227.56 F g^{-1}) to 2:1 (14.97 F g^{-1}) at 1 A g^{-1} reflects an electrochemically resistive threshold. Excessive loading of semiconducting ZnO nanoparticles leads to agglomeration, clogging the micro- and mesoporous channels of the carbon substrate and breaking conductive percolation pathways. Under galvanostatic polarization, this manifests as a large internal iR drop, restricting ion access to electroactive sites and driving cathodic b-values far below the theoretical limit of 0.5 (b_c = 0.204$ for 3:1).

High-Rate Performance Degradation: As current density scales to 10 A g^{-1}, C_{sp} for the 1:1 sample decreases to 11.68 F g^{-1}, while the 2:1, 3:1, and 4:1 samples collapse to negligible specific capacitance of (0.336 F g^{-1}, 0.310 F g^{-1}, and 0.225 F g^{-1}), respectively. This rate-dependent fade highlights that at elevated charge-discharge rates, mass transport becomes strictly surface-limited, where high internal resistance severely suppresses faradaic contributions. The comparative plot matching C_{sp} (GCD) with b-value kinetics is shown in Figure 14.

In summary, cross-correlating GCD rate capabilities with CV scan-rate data and power-law kinetics confirmed that the 1:1 ZnO: AC ratio provides the optimal balance between high electrical conductivity, accessible porosity, and faradaic active sites required for supercapacitor electrodes.

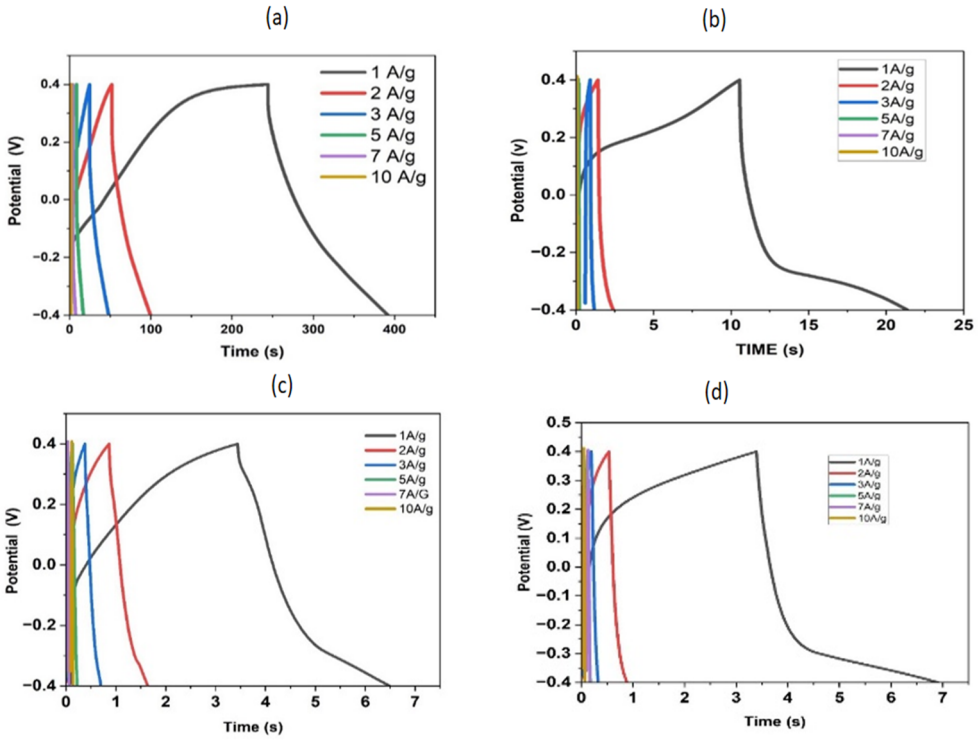


Figure 12. Galvanostatic charge-discharge (GCD) profiles at 1–10 A g^{-1} for the ZnO/AC nanocomposites with the following ratios: (**a**) 1:1 (**b**) 2:1 (**c**) 3:1, and (**d**) 4:1.

Table 4. Gravimetric specific capacitance (C_{sp}, F g^{-1}) of ZnO-AC electrode materials as a function of current density scan rate (1–10 A g^{-1}).

Current Density (A g^{-1})	Specific Capacitance (F g^{-1}) Electrodes Materials			
	ZnO:AC: 1:1	ZnO:AC 2:1	ZnO:AC: 3:1	ZnO:AC 4:1
1	227.56	14.97	3.84	4.30
2	137.15	5.30	2.08	0.94
3	112.76	2.99	1.23	0.51
5	55.76	1.02	0.58	0.31
7	52.86	0.48	0.397	0.28
10	11.68	0.336	0.310	0.225
Retention (1 → 10) (A g^{-1})	5.13%	2.24%	8.07%	5.23%

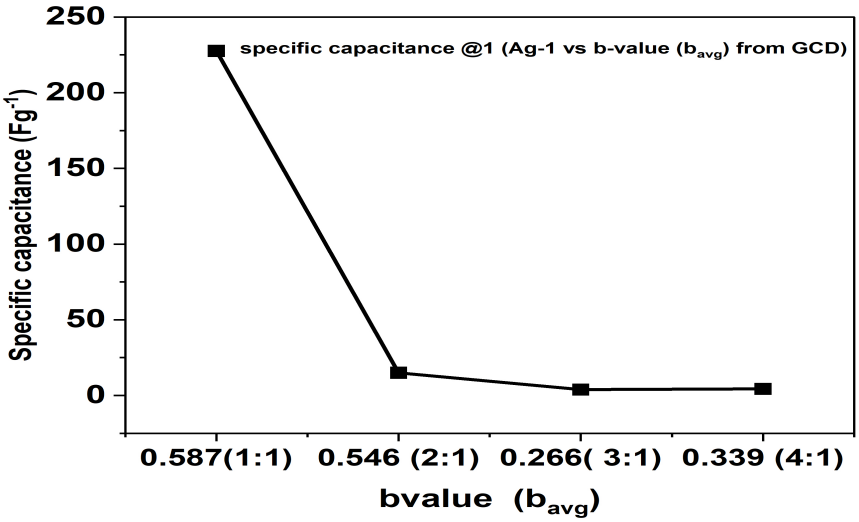


Figure 13. Comparative plot matching C_{sp} (GCD) with b-value kinetics.

To elucidate the fundamental reaction kinetics, charge-transfer resistance, and ion-transport mechanics within the electrode matrix, EIS fitting was performed using an equivalent circuit topology comprising bulk ohmic resistance (*R*1), non-ideal double-layer capacitance (*Q*2, a^2), charge-transfer resistance (*R*2), and finite-length porous diffusion parameters (*Rd*2, *D*2). The extracted kinetic parameters across all mass ratios are summarized in Table 5. The EIS plot is shown in Figure 14.

Table 5. Fitted equivalent circuit parameters for ZnO-AC composites at various mass ratios.

Parameter	ZnO-AC (1:1)	ZnO-AC (2:1)	ZnO-AC (3:1)	ZnO-AC (4:1)
*R*1 (*Rs*) (Ω)	0.3685	0.3153	0.7472	0.3167
*Q*2 (CPE*dl*) F·s^(a^{-1})	3.157×10^{-3}	1.923×10^{-3}	3.553×10^{-3}	1.972×10^{-3}
a^2 (*n*)	0.7052	0.7769	0.5907	0.7784
*R*2 (*Rct*) (Ω)	4.824	20.93	32.14	30.43
*Rd*2 (*Rd*) (Ω)	0.5597	42.84	103.4	46.82
*D*2 (cm^2 s^{-1})	1.072×10^{-9}	2.356×10^{-9}	3.162×10^{-3}	9.810×10^{-8}

The high-frequency real-axis intercept (*R*1) measures the combined uncompensated bulk electrolyte resistance, intrinsic electronic resistance of the nanocomposite active mass, and contact resistance at the current collector interface. All formulations exhibit low ohmic resistance (0.315–0.747 Ω), underscoring excellent electrical contact and electrolyte wetting. The slight elevation observed at the 3:1 ratio (0.7472 Ω) indicates localized particle agglomeration, which slightly disrupts the conductive carbon network.

The mid-frequency charge-transfer resistance (*R*2) captures the Faraday redox reaction rate ($Zn^{2+} \leftrightarrow Zn^{+}$) at the electrolyte interface. A dramatic trend emerges across the composite series. ZnO-AC (1:1) exhibits a remarkably small charge-transfer resistance (*R*2 = 4.824 Ω). Increasing the oxide proportion to 2:1, 3:1, and 4:1 causes *R*2 to surge by an order of magnitude to 20.93 Ω, 32.14 Ω and 30.43 Ω, respectively. This is because zinc oxide possesses lower intrinsic electronic conductivity than activated carbon; excessive zinc oxide loading (>50 wt%) introduces severe interfacial polarization barriers. The 1:1 mass ratio therefore shows an optimal compositional threshold where ZnO nanoparticles are uniformly dispersed over the carbon backbone without forming insulating agglomerates, thereby facilitating rapid interfacial electron transport.

The finite-length diffusion resistance (*Rd*2) reflects the hindrance encountered by solvated ions penetrating the inner pore structure. The 1:1 nanocomposite yields an exceptionally low diffusion resistance (*Rd*2 = 0.5597 Ω). The higher oxide ratios demonstrate extreme pore-blocking behavior, with *Rd*2 increasing to 42.84 Ω (2:1), 103.4 Ω (3:1), and 46.82 Ω (4:1), respectively. This happened because in activated carbon, high surface-area micro- and mesopores provide continuous channels for rapid ion transport. At higher ZnO loadings (≥2:1), excess oxide nanoparticles physically obstruct these pore entrances (pore clogging), sharply restricting ion access to the interior matrix. This physical obstruction correlates directly with the sub-theoretical kinetic exponent ($b < 0.5$) observed in CV power-law analysis for higher-ratio composites.

The ZnO-AC 1:1 nanocomposite, in addition to low mass-transfer resistance (*Rd*2 = 0.5597), maintains a physically robust apparent diffusion coefficient of 1.072×10^{-9} cm^2 s^{-1}, consistent with a controlled, hybrid diffusion-intercalation process (b = 0.587). The ZnO-AC 2:1 ratio similarly shows a balanced diffusion coefficient of 2.356×10^{-9} cm^2 s^{-1}. These values align perfectly with expected solid-state ion transport kinetics in hierarchical porous matrices. The elevated *D*2 value for 3:1 despite a huge *Rd*2 of 103.4 Ω stems from structural pore heterogeneity, as corroborated by its low a^2 exponent.

The CPE phase exponent (a^2) (interfacial heterogeneity) varies between 0.59 and 0.78. The lower value for the 3:1 ratio ($a^2 = 0.5907$) confirms severe surface roughness and pore tortuosity, shifting its response closer to a pure Warburg diffusion tail ($n \approx 0.5$).

In summary, EIS fitting quantitatively confirms that the ZnO-AC (1:1) nanocomposite achieves the superior electrochemical performance required for high-rate supercapacitors. By maintaining a synergistic 1:1 mass balance between the pseudocapacitive ZnO phase and the highly porous activated carbon matrix, the electrode minimizes both Faradaic charge-transfer resistance (*R*2 = 4.824 Ω) and pore diffusion limitations (*Rd*2 = 0.5597 Ω), enabling rapid ion/electron transport kinetics.

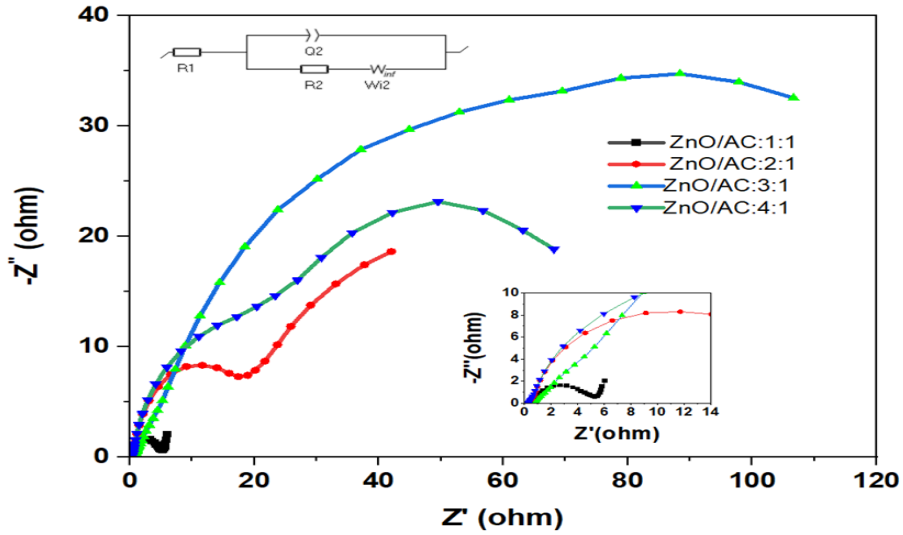


Figure 14. Impedance (EIS) plots for ZnO-AC nanocomposites.

To evaluate the operational durability and phase stability of the electrode materials under prolonged high-rate galvanostatic cycling, long-term charge-discharge tests were performed at a high current density of 10 A g^{-1} up to 3000 continuous cycles as shown in Table 6 and Figure 15.

Table 6. Specific capacitance stability for ZnO-AC composites at 10 A g^{-1}.

Cycle Number	Specific Capacitance Stability (F g^{-1}) at 10 (A g^{-1}) Electrodes Materials			
	ZnO:AC: 1:1	ZnO:AC 2:1	ZnO:AC: 3:1	ZnO:AC 4:1
1	11.7	0.336	0.310	0.225
100	10.3	0.323	0.305	0.238
500	10.1	0.336	0.292	0.238
1000	9.79	0.336	0.297	0.225
1500	9.51	0.336	0.284	0.225
2000	8.70	0.336	0.285	0.225
2500	8.70	0.336	0.284	0.225
3000	8.15	0.336	0.284	0.225
Capacitance Retention (%)	69.66%	100.00%	91.61%	100.00%

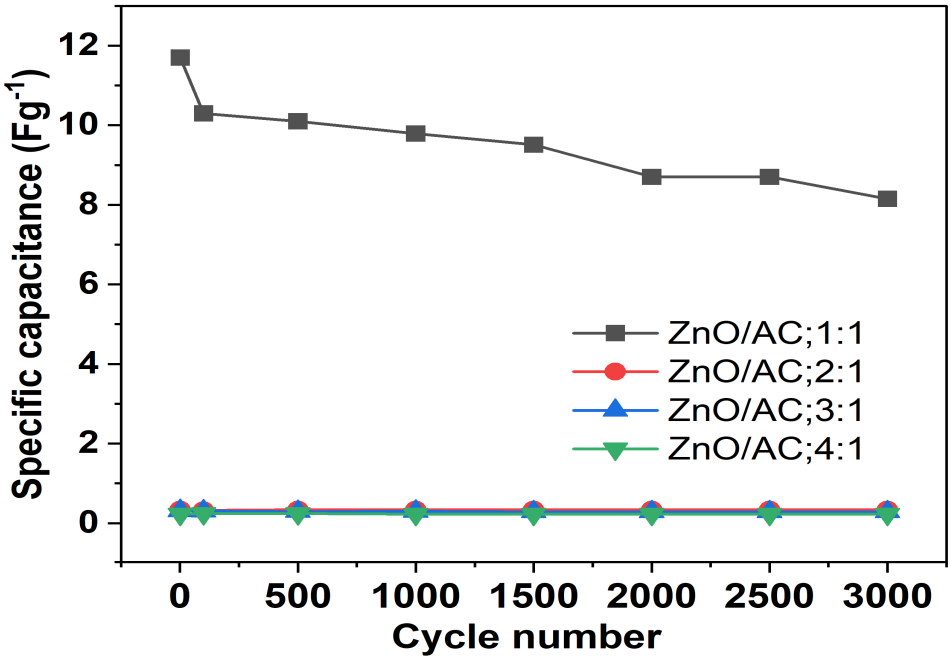


Figure 15. Specific capacitance of ZnO-AC nanocomposites as a function of cycle number-stability at 10 A g^{-1}.

At an ultra-high current density of 10 A g^{-1}, the ZnO: AC (1:1) nanocomposite delivers an initial specific capacitance of 11.70 F g^{-1}, which is 35 to 52 times higher than the specific capacitances delivered by the 2:1 (0.336 F g^{-1}), 3:1 (0.310 F g^{-1}), and 4:1 (0.225 F g^{-1}) samples.

This massive difference in high-rate power output directly correlates with the low charge-transfer resistance ($R2$ = 4.824 Ω) and minimal porous diffusion impedance ($Rd2$ = 0.5597 Ω) established in the EIS analysis. At 10 A g^{-1}, charge-discharge cycles occur within milliseconds. In the higher-ratio formulations (≥2:1), severe pore blockage ($Rd2$ = 42.8–103.4 Ω) restricts ion transport into deep pore channels, rendering the interior active sites inaccessible at high rates.

Over 3000 consecutive cycles, the ZnO:AC (1:1) composite retains 8.15 F g^{-1}, corresponding to a specific capacitance retention of 69.66%.

The observed initial decay phase from (1–1000 cycles) during which, a minor drop from 11.70 F g^{-1} to 9.79 F g^{-1} (16.3% loss) occurs primarily due to the mechanical strain and slight dissolution/surface dissolution-reprecipitation kinetics typical of pseudocapacitive metal oxide nanoparticles during rapid redox transitions (Zn^{2+} ↔ Zn^{+}). Beyond 2000 cycles, the specific capacitance stabilizes completely at 8.70 F g^{-1} → 8.15 F g^{-1}, demonstrating that the robust activated carbon scaffold successfully anchors the ZnO nanoparticles and preserves long-term structural integrity against pulverization.

The 2:1, 3:1, and 4:1 nanocomposite demonstrate flat cycling stability profiles (100% retention for 2:1 and 4:1; 91.6% for 3:1). However, this near-perfect retention occurs at an extremely low magnitude (0.225–0.336 F g^{-1}). This is because ion diffusion into the internal pores of these high-oxide nanocomposites is physically blocked by particle agglomeration (b < 0.50, $Rd2$ > 40 Ω), charge storage occurs exclusively via superficial double-layer adsorption on the outermost geometric surface. Lacking deep Faradaic volume changes or bulk ion intercalation, these surfaces exhibit virtually no structural degradation, albeit at the expense of specific capacitance.

In summary, the cycling stability investigation proves that the ZnO: AC (1:1) composition provides the necessary trade-off between power capability and long-term durability. By delivering a superior discharge capacity (11.70 F g^{-1} at 10 A g^{-1}) alongside 69.66% retention after 3000 high-current cycles, the 1:1 ratio demonstrates strong structural resilience and electrical continuity, confirming its viability for practical fast-charging energy storage applications.

The coulombic efficiency (CE) calculated by considering the charge time (t_c) and discharge time (t_d) at a current density of 10 A g^{-1} according to CE (%) = $\frac{t_d}{t_c} \times 100$ remained around unity throughout cycling, with occasional values slightly exceeding 100% (Table 7 and Figure 16). Such marginal deviations above 100% are generally associated with experimental and calculation uncertainty in determining charge/discharge endpoints, and reversible faradaic processes occurring within porous nanocomposite electrodes. Therefore, values marginally

above 100% should be interpreted as near 100% coulombic efficiency rather than evidence of charge generation. The generally high CE indicates good reversibility of the charge-storage process.

Table 7. Coulombic efficiency for ZnO-AC composites at current density10 A g^{-1}.

Cycle Number	Coulombic Efficiency (%) of Electrodes Materials			
	ZnO:AC: 1:1	ZnO:AC 2:1	ZnO:AC: 3:1	ZnO:AC 4:1
1	101	100	101	100
100	100	100	101	102
500	100	102	100	102
1000	100	102	100	101
1500	100	101	100	101
2000	100	102	100	101
2500	100	102	100	101
3000	100	102	100	101

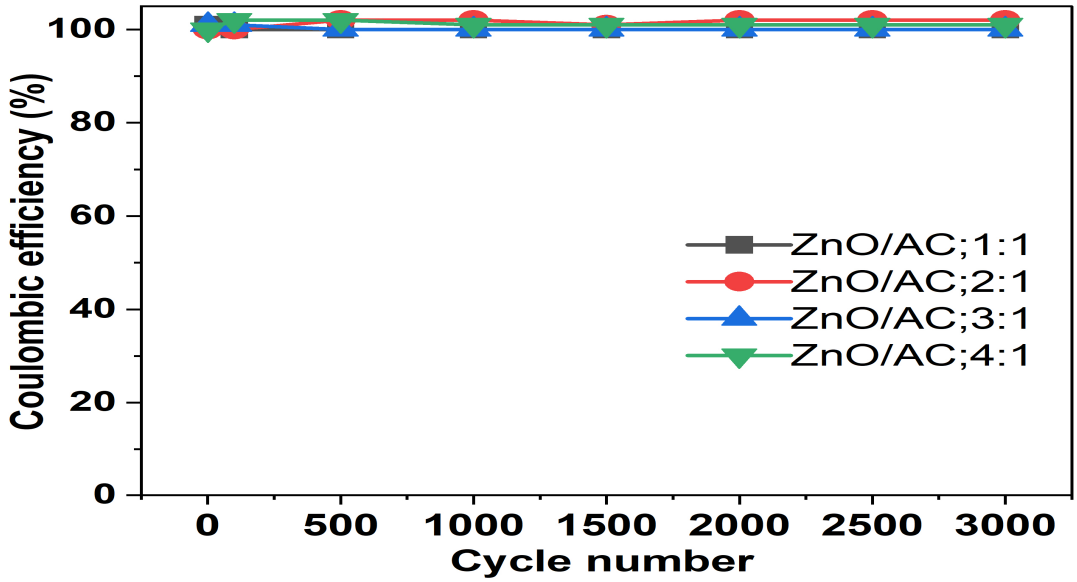


Figure 16. Coulombic efficiency versus cycle number for ZnO-AC nanocomposite at 10 A g^{-1}.

The comparative performance of ZnO-AC alongside previously reported state-of-the-art carbonaceous, metal oxide, and composite supercapacitor materials is summarized in Table 8.

Table 8. Comparative performance of ZnO-AC nanocomposite with literature.

Electrode Materials	Specific Capacitance (Cs) (F/g)	Reference
$ZnMn_2O_4$/MWCNT	103	[29]
AC	105	[43]
25NiO@Co_3O_4-AC	800.9	[43]
25Co_3O_4@NiO-AC	691.8	[43]
Magnetic-activated carbon	76.23	[44]
Activated carbons (ACs)	84	[45]
CHAC	130	[46]
Fe_2O_3/CNT composite	54	[47]
CNT/Fe_3O_4	117.2	[48]
AE-AC	119.97	[28]
AE-AC-doped Fe_3O_4	205.86	[28]
ZnO-AC	322 (CV)	This Work
ZnO-AC	227.56 (GCD)	This Work

The synthesized ZnO-AC hybrid electrode demonstrated comparable performance, delivering a maximum specific capacitance of 322 F g^{-1} calculated via CV (at a sweep rate of 5 mV s^{-1}) and 227.56 F g^{-1} evaluated via GCD at a current density of 1 A g^{-1}.

As shown in Table 8, standard pristine activated carbons (ACs) typically exhibit moderate electrical double-layer capacitance (EDLC) due to electrostatic ion adsorption within micro/mesoporous networks, yielding values between 84 F g^{-1} and 105 F g^{-1} [43,45]. Chemical modification or functionalization, AE-AC 119.97 F g^{-1} [28] or

magnetic activation 76.23 F g^{-1} [44] offers minor enhancements but remains fundamentally constrained by the electrostatic charge storage ceiling of carbon double layers.

Incorporating ZnO nanostructures onto the activated carbon substrate in this work dramatically enhances charge storage capability, boosting the GCD-based specific capacitance to 227.56 F g^{-1}, a 116–170% increase over pristine and modified carbon frameworks. This enhancement highlights the effective integration of faradaic pseudo capacitance from the transition metal oxide phase without sacrificing the carbon matrix's structural integrity and accessible surface area.

When benchmarked against existing metal oxide/carbon nanotube (CNT) and multi-walled carbon nanotube (MWCNT) hybrids, the (ZnO-AC) composite consistently outperforms several established materials: Fe_2O_3/CNT (54 F g^{-1}) [47], $ZnMn_2O_4$/MWCNT (103 F g^{-1}) [29], CNT/Fe_3O_4 (117.20 F g^{-1}) [48] AE-AC-doped Fe_3O_4 (205.86 F g^{-1}) [28].

The pronounced specific capacitance of ZnO-AC over iron- and manganese oxide-based hybrids stems from the favorable surface redox kinetics of nanostructured ZnO coupled with the high electrical conductivity of the porous carbon matrix, which minimizes internal ohmic losses (R_s) and facilitates rapid interfacial charge transfer.

Core-shell bimetallic oxides, such as 25NiO@Co_3O_4-AC (800.9 F g^{-1}) and 25Co_3O_4@NiO-AC (691.8 Fg^{-1}) [43], achieve higher absolute specific capacitance values due to multi-electron redox transition numbers (Ni^{2+}/Ni^{3+} and $Co^{2+}/Co^{3+}/Co^{4+}$). However, cobalt- and nickel-based systems face severe practical constraints, including high toxicity, elevated precursor costs, and significant structural strain during continuous cycling. In contrast, ZnO-AC presents a non-toxic, eco-benign, highly abundant, and economically viable alternative that maintains excellent operational electrochemical performance.

4. Conclusions

Developing good-performance, low-cost electrode materials from renewable resources is crucial for advancing sustainable electrochemical energy storage devices. In this work, we report a sustainable, circular-economy-driven synthesis of nanocomposite supercapacitor electrodes utilizing rice husk ash (RHA), a waste-derived and potentially greener route to ZnO and activated carbon (AC) prepared from unripe plantain peels. The structural, textural, and electrochemical properties of the bio-waste-derived ZnO-AC nanocomposites were systematically investigated across four mass ratios. X-ray diffraction (XRD) confirmed the successful phase integration of hexagonal wurtzite ZnO, identified by prominent diffraction planes including (100), (002), (101), (102), (110), and (112), anchored to the amorphous graphitic matrix of plantain-peel AC. Brunauer–Emmett–Teller (BET) analysis revealed that introducing unripe plantain-peel AC into the RHA-derived ZnO matrix significantly enhances textural properties, peaking at an optimal surface area of 659.556 m^2, a pore volume of 0.582 cm^3, and an average mesopore diameter of 3.02 nm for the 2:1 ZnO-AC composite. The fundamental charge-storage kinetics of zinc oxide/activated carbon (ZnO/AC) nanocomposites for supercapacitor electrodes were investigated.

Through comprehensive cyclic voltammetry (CV), Galvanostatic Charge-Discharge (GCD), and Electrochemical Impedance Spectroscopy (EIS), we demonstrated that electrochemical performance is critically governed by the active mass ratio between the pseudocapacitive metal oxide and the conductive carbon matrix.

The ZnO-AC (1:1) nanocomposite emerged as the optimal formulation, delivering a maximum specific capacitance of 227.56 F g^{-1} at 1 A g^{-1} and maintaining superior high-rate capability (11.70 F g^{-1}) at an ultra-high current density of 10 A g^{-1}. Kinetic power-law analysis confirmed a balanced hybrid mechanism (b = 0.587), wherein rapid surface EDLC accumulation synergizes with Faradaic redox kinetics ($Zn^{2+} \leftrightarrow Zn^{+}$). EIS fitting using $R1 + Q2/(R2 + W2)$ circuit model physically substantiated these kinetic trends. The 1:1 architecture minimizes both charge-transfer resistance ($R2$ = 4.824 Ω) and porous ion-diffusion resistance ($Rd2$ = 0.5597 Ω). Conversely, exceeding 50 wt% oxide content (≥2:1) induces severe particle agglomeration and pore clogging, increasing diffusion impedance by up to two orders of magnitude ($Rd2$ = 103.4 Ω) and restricting performance to sub-theoretical regimes (b < 0.50). Furthermore, the 1:1 material demonstrated reasonable operational durability, retaining 69.66% of its initial high-rate capacity over 3000 continuous charge-discharge cycles.

5. Limitations and Future Perspectives

Despite these promising material-level kinetics, two primary limitations must be addressed to translate these nanocomposites into commercial energy storage technologies:

1 Intrinsic Electronic Conductivity of Zinc Oxide: While the 1:1 composite ratio mitigates polarization barriers, the wide bandgap and modest intrinsic conductivity of ZnO restrict ultimate rate capability compared to transition metal nitrides or carbon-rich pseudo capacitors. Future material design could explore heteroatom doping (e.g., N, S, or Al doping in ZnO) or oxygen-vacancy engineering to elevate intrinsic electronic conductivity.

2 Device-Level Integration and Practical Validation: A key limitation of the present study is its exclusive focus on half-cell material characterization (3-electrode setup) in an aqueous electrolyte environment. Half-cell metrics evaluate intrinsic material performance under ideal flooding conditions but do not account for practical device constraints such as mass matching, cell balancing, separator resistance, and packaging dead weight.

To bridge the gap between fundamental material chemistry and practical implementation, future efforts will focus on fabricating full asymmetric supercapacitor (ASC) coin/pouch cells pairing the optimized ZnO/AC (1:1) positive electrode with a suitable high-surface-area negative electrode (e.g., pure AC or MXenes) in wide-voltage aqueous or ionic liquid electrolytes. This work provides the fundamental kinetic baseline and compositional framework required to guide such real-world energy storage device design.

Author Contributions

P.I.O.: Conceptualization, methodology, writing—original draft preparation, visualization and investigation; I.S.I.: Writing—original draft preparation, supervision, writing—reviewing and editing; E.E.K.: Supervision, writing—reviewing and editing; F.L.K.: Supervision, writing—reviewing and editing; S.O.O.: Writing—original draft preparation; M.A.K.: Supervision, writing—reviewing and editing; A.B.: Supervision, writing—reviewing and editing. All authors have read and agreed to the published version of the manuscript.

Funding

This research received no external funding.

Institutional Review Board Statement

Not applicable.

Informed Consent Statement

Not applicable.

Data Availability Statement

The authors are ready to provide the raw data of their study and are prepared to make the data publicly other competent professionals for at least 10 years after publication (preferably via an institutional or subject-based data repository or other data center), provided that the confidentiality of the participants can be protected and legal rights concerning proprietary data do not preclude their release.

Acknowledgments

I acknowledge with gratitude the support received from the research laboratories, analytical facilities, and technical personnel of African University of Science and Technology (AUST) and Nano Laboratory University of Nigeria, Nsukka (UNN) who assisted with the experimental and characterization aspects of this work. The technical expertise and willingness of Emmanuel of African University of Science and Technology (AUST), Qkparaku, Emil and Richard of the University of Nigeria, Nsukka (UNN), to assist were invaluable to the successful completion of the experimental work.

Conflicts of Interest

The authors declare no conflict of interest.

Use of AI and AI-Assisted Technologies

No AI tools were utilized for this paper.

References

1. Miller, J.R.; Simon, P. The Chalkboard: Fundamentals of Electrochemical Capacitor Design and Operation. *Electrochem. Soc. Interface* **2008**, *17*, 31–32. https://doi.org/10.1149/2.f02081if.
2. Mensah-Darkwa, K.; Zequine, C.; Kahol, P.K.; et al. Supercapacitor Energy Storage Device Using Biowastes: A Sustainable Approach to Green Energy. *Sustainability* **2019**, *11*, 414. https://doi.org/10.3390/su11020414.

3. Poonam; Sharma, K.; Arora, A.; et al. Review of supercapacitors: Materials and devices. *J. Energy Storage* **2019**, *21*, 801–825. https://doi.org/10.1016/j.est.2019.01.010.
4. Simon, P.; Gogotsi, Y. Materials for electrochemical capacitors. *Nat. Mater.* **2008**, *7*, 845–854. https://doi.org/10.1038/nmat2297.
5. Frackowiak, E.; Khomenko, V.; Jurewicz, K.; et al. Supercapacitors based on conducting polymers/nanotubes composites. *J. Power Sources* **2006**, *153*, 413–418. https://doi.org/10.1016/j.jpowsour.2005.05.030.
6. Dissanayake, K.; Kularatna-Abeywardana, D. A review of supercapacitors: Materials, technology, challenges, and renewable energy applications. *J. Energy Storage* **2024**, *96*, 112563. https://doi.org/10.1016/j.est.2024.112563.
7. Miller, E.E.; Hua, Y.; Tezel, F.H. Materials for energy storage: Review of electrode materials and methods of increasing capacitance for supercapacitors. *J. Energy Storage* **2018**, *20*, 30–40. https://doi.org/10.1016/j.est.2018.08.009.
8. Gorgulu, S.C.; Yazar, I.; Karakoc, T.H. Review of supercapacitor technology and applications. *J. Mechatron. Artif. Intell. Eng.* **2024**, *5*, 131–143. https://doi.org/10.21595/jmai.2024.24103.
9. Tshiani, C.T.; Umenne, P. The Impact of the Electric Double-Layer Capacitor (EDLC) in Reducing Stress and Improving Battery Lifespan in a Hybrid Energy Storage System (HESS) System. *Energies* **2022**, *15*, 8680. https://doi.org/10.3390/en15228680.
10. Kumar, Y.; Sharma, S.; Pullabhotla, V.R. Electrochemical Characterizations of Electrode Materials for Supercapacitors. *Mater. Int.* **2025**, *7*, 10. https://doi.org/10.33263/materials71.010.
11. Liu, H.; Zhang, L. Pore-structure control of porous carbon electrode materials and energy-storage performance in water-in-salt electrolytes. *J. Electroanal. Chem.* **2024**, *961*, 118233. https://doi.org/10.1016/j.jelechem.2024.118233.
12. Noukelag, S.K.; Mohamed, H.E.A.; Moussa, B.; et al. Investigation of structural and optical properties of biosynthesized Zincite (ZnO) nanoparticles (NPs) via an aqueous extract of Rosmarinus officinalis (rosemary) leaves. *MRS Adv.* **2020**, *5*, 2349–2358. https://doi.org/10.1557/adv.2020.220.
13. Forouzandeh, P.; Kumaravel, V.; Pillai, S.C. Electrode Materials for Supercapacitors: A Review of Recent Advances. *Catalysts* **2020**, *10*, 969. https://doi.org/10.3390/catal10090969.
14. Sharma, R.K.; Rastogi, A.C.; Desu, S.B. Manganese oxide embedded polypyrrole nanocomposites for electrochemical supercapacitor. *Electrochim. Acta* **2008**, *53*, 7690–7695. https://doi.org/10.1016/j.electacta.2008.04.028.
15. Selvakumar, M.; Krishna Bhat, D.; Aggarwal, A.M.; et al. Nano ZnO-activated carbon composite electrodes for supercapacitors. *Phys. B Condens. Matter* **2010**, *405*, 2286–2289. https://doi.org/10.1016/j.physb.2010.02.028.
16. Pradeep, M.; Panwar, N.L.; Divyangkumar, N. Torrefaction of agricultural biomass: A state-of-the-art review on transforming waste into clean energy. *Energy 360* **2025**, *3*, 100023. https://doi.org/10.1016/j.energ.2025.100023.
17. Samage, A.; Halakarni, M.; Yoon, H.; et al. Sustainable conversion of agricultural biomass waste into electrode materials with enhanced energy density for aqueous zinc-ion hybrid capacitors. *Carbon* **2024**, *219*, 118774. https://doi.org/10.1016/j.carbon.2023.118774.
18. Ngom, I.; Ndiaye, N.M.; Fall, A.; et al. On the Use of Moringa Oleifera Leaves Extract for the Biosynthesis of NiO and ZnO Nanoparticles. *MRS Adv.* **2020**, *5*, 1145–1155. https://doi.org/10.1557/adv.2020.212.
19. Yadav, M.S.; Singh, N.; Bobade, S.M. Zinc oxide nanoparticles and activated charcoal-based nanocomposite electrode for supercapacitor application. *Ionics* **2018**, *24*, 3611–3630. https://doi.org/10.1007/s11581-018-2527-1.
20. Raja, V.; Selvan, G.; Anbarasu, R.; et al. Green synthesis of zinc oxide nanoparticles using Hyptis leaf extract and Activated carbon based Zinc oxide composite of Supercapacitor Applications. *Indian J. Sci. Technol.* **2019**, *12*, 107–108. https://doi.org/10.17485/ijst/2019/v12i40/148040.
21. Mohamed, I.M.A.; Yasin, A.S.; Liu, C. Synthesis, surface characterization and electrochemical performance of ZnO @ activated carbon as a supercapacitor electrode material in acidic and alkaline electrolytes. *Ceram. Int.* **2020**, *46*, 3912–3920. https://doi.org/10.1016/j.ceramint.2019.10.119.
22. Gorgulu, S.C.; Yazar, I.; Karakoc, T.H. Energy storage technologies and their combinational usage in micro/mini unmanned aerial vehicles: A review. *J. Mechatron. Artif. Intell. Eng.* **2024**, *5*, 72–88. https://doi.org/10.21595/jmai.2024.24104.
23. Taer, E.; Taslim, R.; Aini, Z.; et al. Activated carbon electrode from banana-peel waste for supercapacitor applications. In Proceedings of the 6th International Conference on Theoretical and Applied Physics (The 6th ICTAP), Makassar, Indonesia, 19–21 September 2016; Vol. 1801, p. 040004. https://doi.org/10.1063/1.4973093.
24. Wang, Y.; Wu, X.; Han, Y.; et al. Flexible supercapacitor: Overview and outlooks. *J. Energy Storage* **2021**, *42*, 103053. https://doi.org/10.1016/j.est.2021.103053.
25. Saka, C.; Levent, A. Fabrication of nitrogen and ZnO doped on carbon particles obtained from waste biomass and their use as supercapacitor electrodes for energy storage. *Int. J. Hydrogen Energy* **2024**, *90*, 1070–1083. https://doi.org/10.1016/j.ijhydene.2024.10.061.
26. Madhu, R.; Veeramani, V.; Chen, S.M.; et al. Functional porous carbon–ZnO nanocomposites for high-performance biosensors and energy storage applications. *Phys. Chem. Chem. Phys.* **2016**, *18*, 16466–16475. https://doi.org/10.1039/c6cp01285j.

27. Öziç, C.; Baran, M.F.; Levent, A.; et al. Green synthesis and electroanalytical characterization of Ocimum basilicum-functionalized ZnO nanoparticles for supercapacitor electrode applications. *Microchem. J.* **2026**, *227*, 118675. https://doi.org/10.1016/j.microc.2026.118675.
28. Aslan, K.S.; Ertaş, E.; Baran, M.F.; et al. Enhanced Electrochemical Performance of Supercapacitors Using Fe3O4-Doped Biomass-Derived Activated Carbon Electrodes. *Electrochem. Sci. Adv.* **2026**, *6*, e70014. https://doi.org/10.1002/elsa.70014.
29. Aruchamy, K.; Nagaraj, R.; Manohara, H.M.; et al. One-step green route synthesis of spinel ZnMn2O4 nanoparticles decorated on MWCNTs as a novel electrode material for supercapacitor. *Mater. Sci. Eng. B* **2020**, *252*, 114481. https://doi.org/10.1016/j.mseb.2019.114481.
30. Ma, Y.; Yin, J.; Liang, H.; et al. A two step approach for making super capacitors from waste wood. *J. Clean. Prod.* **2021**, *279*, 123786. https://doi.org/10.1016/j.jclepro.2020.123786.
31. Palavai, S.S.; Awasthi, H.; Goel, S. Scalable hematite based symmetric supercapacitor with high capacitance for energy storage applications. *Front. Batter. Electrochem.* **2026**, *5*, 1795529. https://doi.org/10.3389/fbael.2026.1795529.
32. Liu, Z.; Ye, D.; Zhu, X.; et al. ZIF-67-derived Co nanoparticles embedded in N-doped porous carbon composite interconnected by MWCNTs as highly efficient ORR electrocatalysts for a flexible direct formate fuel cell. *Chem. Eng. J.* **2022**, *432*, 134192. https://doi.org/10.1016/j.cej.2021.134192.
33. Zhang, L.; Shi, D.; Liu, T.; et al. Nickel-based materials for supercapacitors. *Mater. Today* **2019**, *25*, 35–65. https://doi.org/10.1016/j.mattod.2018.11.002.
34. An, C.; Zhang, Y.; Guo, H.; et al. Metal oxide-based supercapacitors: Progress and prospectives. *Nanoscale Adv.* **2019**, *1*, 4644–4658. https://doi.org/10.1039/c9na00543a.
35. Xiao, S.; Huang, J.; Lin, C.; et al. Porous carbon derived from rice husks as sustainable bioresources: Insights into the role of micro/mesoporous hierarchy in Co_3O_4/C composite for asymmetric supercapacitors. *Microporous Mesoporous Mater.* **2020**, *291*, 109709. https://doi.org/10.1016/j.micromeso.2019.109709.
36. Dong, Y.; Wang, Y.; Xu, Y.; et al. Facile synthesis of hierarchical nanocage $MnCo_2O_4$ for high performance supercapacitor. *Electrochim. Acta* **2017**, *225*, 39–46. https://doi.org/10.1016/j.electacta.2016.12.109.
37. Salunkhe, R.R.; Kaneti, Y.V.; Yamauchi, Y. Metal–Organic Framework-Derived Nanoporous Metal Oxides toward Supercapacitor Applications: Progress and Prospects. *ACS Nano* **2017**, *11*, 5293–5308. https://doi.org/10.1021/acsnano.7b02796.
38. Wang, F.; Wu, X.; Yuan, X.; et al. Latest advances in supercapacitors: From new electrode materials to novel device designs. *Chem. Soc. Rev.* **2017**, *46*, 6816–6854. https://doi.org/10.1039/c7cs00205j.
39. Kuo, T.R.; Lin, L.Y.; Kubendhiran, S.; et al. Novel incorporation of redox active organic molecule with activated carbon as efficient active material of supercapacitors. *J. Energy Storage* **2022**, *53*, 105085. https://doi.org/10.1016/j.est.2022.105085.
40. Zhang, W.; Pan, Y.; Wang, H.; et al. Preparation and Characterization of High-Performance Fe3O4/RGO Anode for Supercapacitors. *J. Electron. Mater.* **2023**, *52*, 6107–6120. https://doi.org/10.1007/s11664-023-10552-1.
41. Potham, S.; Ramanujam, K. A novel hierarchical porous activated carbon-organic composite cathode material for high performance aqueous zinc-ion hybrid supercapacitors. *J. Power Sources* **2023**, *557*, 232551. https://doi.org/10.1016/j.jpowsour.2022.232551.
42. Saka, C.; Levent, A. High-performance pseudo-capacitance supercapacitor with highly mesoporous fluorine doped polymeric carbon nitride nanosheets as electrode material. *Diam. Relat. Mater.* **2024**, *148*, 111504. https://doi.org/10.1016/j.diamond.2024.111504.
43. Gouda, M.S.; Shehab, M.; Helmy, S.; et al. Nickel and cobalt oxides supported on activated carbon derived from willow catkin for efficient supercapacitor electrode. *J. Energy Storage* **2023**, *61*, 106806. https://doi.org/10.1016/j.est.2023.106806.
44. Ozpinar, P.; Dogan, C.; Demiral, H.; et al. Activated carbons prepared from hazelnut shell waste by phosphoric acid activation for supercapacitor electrode applications and comprehensive electrochemical analysis. *Renew. Energy* **2022**, *189*, 535–548. https://doi.org/10.1016/j.renene.2022.02.126.
45. Adan-Mas, A.; Alcaraz, L.; Arévalo-Cid, P.; et al. Coffee-derived activated carbon from second biowaste for supercapacitor applications. *Waste Manag.* **2021**, *120*, 280–289. https://doi.org/10.1016/j.wasman.2020.11.043.
46. Raj, C.J.; Manikandan, R.; Rajesh, M.; et al. Cornhusk mesoporous activated carbon electrodes and seawater electrolyte: The sustainable sources for assembling retainable supercapacitor module. *J. Power Sources* **2021**, *490*, 229518. https://doi.org/10.1016/j.jpowsour.2021.229518.
47. Xu, C.H.; Shen, P.Y.; Chiu, Y.F.; et al. Atmospheric pressure plasma jet processed nanoporous Fe_2O_3/CNT composites for supercapacitor application. *J. Alloys Compd.* **2016**, *676*, 469–473. https://doi.org/10.1016/j.jallcom.2016.03.185.
48. Guan, D.; Gao, Z.; Yang, W.; et al. Hydrothermal synthesis of carbon nanotube/cubic Fe_3O_4 nanocomposite for enhanced performance supercapacitor electrode material. *Mater. Sci. Eng. B* **2013**, *178*, 736–743. https://doi.org/10.1016/j.mseb.2013.03.010.